Title: Membrane-associated periodic skeleton regulates major forms of endocytosis in neurons through a signaling-driven positive feedback loop

Authors: Jinyu Fei[1], Yuanmin Zheng[2], Caden LaLonde[3], Yuan Tao[4], Ruobo Zhou[1,2,3,4,*]

Affiliations:

[1] Department of Chemistry, The Pennsylvania State University, University Park, PA 16802, USA

[2]Department of Biomedical Engineering, The Pennsylvania State University, University Park, PA 16802, USA

[3]Department of Biochemistry and Molecular Biology, The Pennsylvania State University, University Park, PA 16802, USA

[4]The Huck Institutes of Life Sciences, The Pennsylvania State University, University Park, PA 16802, USA

* To whom correspondence may be addressed. Email: ruobo.zhou@psu.edu

Abstract

Endocytosis enables neurons to internalize molecules, maintaining homeostasis and responsiveness. The neuronal membrane-associated periodic skeleton (MPS), an actin-spectrin-based cytoskeletal lattice, is known to restrict clathrin-mediated endocytosis (CME) in axons, but its broader role in other neuronal compartments and endocytic pathways remains unclear. Here, we show that all four major endocytic pathways—CME, caveolin-, flotillin-, and fast endophilin-mediated endocytosis—are spatially gated by the MPS and occur exclusively within MPS-free "clearing" zones throughout all neuronal compartments. Disrupting the MPS broadly enhances both basal and ligand-induced endocytosis. We also identify a novel feedback loop in which ligand-triggered endocytosis activates ERK signaling, promoting protease-mediated spectrin cleavage and MPS disruption, which in turn facilitates further endocytosis. Furthermore, the MPS limits amyloid precursor protein endocytosis, thereby suppressing Aβ42 production and linking MPS integrity to neurodegeneration. Our findings establish the MPS as a dynamic, signal-responsive modulator coupling membrane trafficking with cortical cytoskeletal organization and neuronal health.

Introduction

Endocytosis is a fundamental and evolutionarily conserved cellular process, essential for a wide range of organisms, including yeast, animals, and plants(*1*). It plays a critical role in maintaining the homeostasis of cell membrane constituents by recycling specific lipid and protein components of the plasma membrane and in facilitating the cell's nutrient uptake and communication with its extracellular environment and neighboring cells by internalizing and sampling extracellular materials, such as fluids, biomolecules, and microbes. In neurons, endocytosis regulates nerve cell migration and adhesion during brain development, establishes neuronal differentiation and axon-dendrite polarity, and governs synaptic activity and plasticity by controlling synaptic transmission and shaping the size, structure, and number of synapses, thereby influencing brain development, functions, and activities such as learning and memory(*2*). Conversely, dysregulation of endocytosis has been implicated in the pathogenesis of various neurological disorders(*3-5*). Genetic studies have identified mutations which alter the expression of endocytic machinery genes in neurodegenerative diseases such as Alzheimer's disease, Parkinson's disease, and amyotrophic lateral sclerosis(*6*).

The regulation of endocytosis relies on the intricate interplay of protein-specific interactions, signaling pathway activation, and cytoskeleton rearrangement. While significant progress has been made in understanding the molecular mechanisms underlying endocytic pathways(*1, 7*), many aspects of the molecular mechanisms underlying neuronal endocytosis remain poorly understood. To facilitate the uptake of diverse extracellular materials, various distinct endocytic mechanisms have been identified in non-neuronal cells, including clathrin-mediated endocytosis (CME, a clathrin- and dynamin-dependent pathway), lipid raft-mediated endocytosis (LRME, a clathrin-independent but dynamin-dependent pathway), fast endophilin-mediated endocytosis (FEME, a clathrin-independent but dynamin-dependent pathway for rapid ligand-driven internalization of specific membrane proteins), macropinocytosis, and phagocytosis(*1, 7*). Among these, CME is the most well-studied endocytic pathway in neurons and has been shown to occur ubiquitously across nearly all neuronal subcompartments, including the soma, axon shaft, dendrite shaft, and both pre- and post-synaptic sites. In contrast, much less is known about the localization and regulation of other endocytic pathways in neurons. These pathways are functionally complementary rather than redundant: although they can internalize overlapping membrane regions, each is defined by distinct molecular machineries, cargo preferences, regulatory mechanisms, temporal dynamics, and their precise contributions to neuronal homeostasis, plasticity, and signaling(*8-13*), underscoring their unique and essential roles within the complex neuronal environment.

A decade ago, super-resolution imaging enabled the discovery of the neuronal actin-spectrin-based membrane-associated periodic skeleton (MPS), a structure in which actin filaments are organized into

“rings” connected by spectrin tetramers, forming a one-dimensional (1D) periodic lattice with ~190-nm spacing beneath the plasma membrane of neurites(*14*). In mature neurons, the MPS extends throughout ~90% of axonal regions, including both the axon initial segment and distal axons(*14-16*), and is also observed in ~50% of dendritic regions(*15, 17, 18*). The MPS is broadly distributed across diverse neuronal types, including excitatory and inhibitory neurons in both the central and peripheral nervous systems(*19, 20*), and is conserved across species ranging from *C. elegans* to humans(*20*). This submembrane cytoskeletal network plays a critical role in organizing transmembrane proteins, such as ion channels, adhesion molecules, membrane transporters and receptors(*14, 15, 17, 21-24*). The MPS has been implicated in enhancing axonal stability under mechanical stress(*14, 25*), mediating mechanosensation(*26*), controlling neurite diameter and bundling(*27*), influencing axon degeneration(*28, 29*), and regulating neuronal receptor signaling(*23*) and CME(*23, 30*), emphasizing its essential role in neuronal function and health.

A recent study has reported a novel cell surface-localized structure in neurons, termed “clearings”, which regulates CME at the axon initial segment (AIS) and proximal axon segments near the AIS(*30*). These “clearings” are empty, membrane-associated holes surrounded by the actin-spectrin-based MPS network. Clathrin-coated pits (CCPs) preferentially form at the center of these pre-existing “clearings” and are stabilized as long-lived and stalled structures before undergoing scission and conclusive endocytosis in response to plasticity-inducing stimulation. Despite these insights, several critical questions remain unresolved. First, although the initial study reports that the “clearings” of the MPS scaffold exclusively formed at AIS and proximal axon next to AIS and were absent from soma and dendrites, this observation was made using relatively immature neurons at 14 days in vitro (DIV 14), when the MPS has not fully developed in the somatodendritic compartments(*18*). Our previous systematic investigation of the developmental progression of the MPS demonstrated that MPS formation occurs much slower in somatodendrites than in axons, with the MPS network density in soma and dendrites reaching saturation only around DIV 21-28(*18*). Therefore, it remains an open question whether similar CCP-containing "clearings" exist in distal axons or somatodendritic compartments in more mature (DIV 21 or older) neurons. Second, whether clathrin-independent endocytic pits, such as those involved in LRME or FEME, also preferentially localize to the centers of MPS-free clearings, and whether their endocytic activity is similarly regulated by the MPS, have not been investigated. Third, the mechanisms that control the formation, size, and spatial distribution of these clearings in response to increased endocytic demand, such as during neuronal stimulation, are largely unexplored. Given that the MPS inhibits ligand-induced CME, a critical unresolved question is how the MPS is locally disassembled, through the formation or expansion of clearings, to accommodate elevated endocytic activity during periods of rapid neuronal signaling.

Here, using super-resolution fluorescence microscopy(*31, 32*) in combination with quantitative cell biology approaches, we systematically investigated four major types of endocytosis in neurons: CME, caveolin-mediated endocytosis and flotillin-mediated endocytosis(*33*) (two prominent forms of LRME), and FEME(*12*). Similar to CME, we found that caveolin-mediated endocytosis, flotillin-mediated endocytosis, and endophilin-mediated endocytosis (i.e., FEME) can occur broadly across nearly all neuronal compartments, including the soma, AIS, axon shaft, and dendrite shaft. Notably, we identified CCP-centered clearings not only in the proximal axon shaft as previously reported(*30*), but also in distal axons and somatodendritic regions of mature neurons. For the other three types of endocytic pathways, we identified analogous "clearings" formed by the actin-spectrin-based MPS, with caveolin-, flotillin-, or endophilin-enriched nanodomains located at their centers, resembling the previously reported CCP-centered clearings. Disruption of the neuronal MPS enhanced both basal endocytosis mediated by clathrin, caveolin, flotillin, and endophilin, as well as ligand-induced receptor endocytosis across these pathways. These findings suggest that the MPS serves as a physical barrier to suppress endocytosis for all the four endocytosis types. We further demonstrated that ligand-induced receptor endocytosis mediated by these proteins activates downstream ERK signaling cascades and proteases (i.e., calpains and caspases), which in turn can promote MPS disassembly (i.e., enlarge the total area of "clearings"), forming a positive feedback loop that further enhances endocytosis. These findings indicate that the MPS acts as a dynamically regulated barrier to modulate endocytosis rates. Finally, we demonstrated that the MPS exerts a neuroprotective role by negatively regulating amyloid precursor protein (APP) endocytosis through the same positive feedback loop. Given that APP endocytosis is upregulated during neuronal aging and in Alzheimer's disease(*3, 4*), this MPS-mediated regulation may serve as a protective mechanism against disease-associated endocytic dysregulation. Together, these findings provide structural and mechanistic insights into the regulation of diverse neuronal endocytosis pathways under both physiological and pathological conditions.

Results

Compartment-resolved mapping of four endocytic pit types reveals broad suppression of basal endocytosis by the neuronal MPS

As studies of neuronal endocytosis have primarily focused on CME and it remains largely unclear which neuronal compartments support other endocytic pathways, we first sought to develop immunofluorescence (IF)-based assays capable of accurately mapping the spatial distributions of four major types of endocytic pits, including the endocytic pits for CME (i.e., CCPs), caveolin-mediated endocytosis, flotillin-mediated endocytosis, and FEME, respectively, across different neuronal compartments. In cells, CME serves as the major constitutive "housekeeping" pathway, continuously

sampling the extracellular environment and mediating the bulk uptake of diverse cargoes such as nutrients, antigens, and signaling receptors. It is critical for maintaining cellular homeostasis and regulating signal transduction across various cell types(*8*). Caveolin-mediated endocytosis is less involved in bulk uptake and more specialized in organizing signal transduction and lipid regulation through flask-shaped membrane invaginations called caveolae. It specializes in internalizing specific lipids and certain toxins(*9, 10*). Flotillin-mediated endocytosis functions through clathrin- and caveolin-independent, microdomain-associated vesicles formed by flotillin scaffolds. This pathway mediates the uptake of selected membrane proteins and contributes to cytoskeletal organization and receptor recycling(*11*). FEME represents a rapid, activity-dependent route that enables the efficient internalization of activated surface receptors upon ligand binding, thereby supporting swift cellular responses and dynamic signaling modulation(*12, 13*). Together, these pathways form a complex yet complementary network that allows cells to precisely regulate the internalization of external materials and membrane proteins, facilitating adaptation to diverse physiological demands and environmental cues. Consequently, mapping their spatial distribution across different neuronal subcompartments can provide a comprehensive framework for understanding the endocytic landscape in neurons. While the IF staining protocol for visualizing CCPs in neurons has been well documented(*30*), staining protocols for other endocytic pits in neurons are underdeveloped. Previous studies have reported that the commonly used cell permeabilization method using Triton X-100 substantially alters the staining patterns of lipid-raft-mediated endocytic pits(*34*). To overcome this, we expressed moderate level of GFP-tagged caveolin-1(Cav1), flotillin-1 (Flot1), or endophilin-A2 (EndoA2) in cultured neurons through low-titer lentiviral transduction, and tested IF protocols previously developed for non-neuronal systems(*12, 33-35*) (**Fig. S1**). Neurons were immunostained with IF-validated antibodies against endogenous Cav1(*35*), Flot1(*33*), and EndoA2(*12*), respectively. The observed strong colocalization between immunostained puncta and the puncta in the GFP channel, which are likely endocytic pits, confirmed the specificity of these antibodies and validated the IF-based assays for visualizing these endocytic pits in neuronal systems.

Using these IF-based assays, with immunostaining for endogenous clathrin, Cav1, Flot1, and EndoA2, and structured illumination microscopy (SIM)(*36, 37*), a super-resolution imaging method with a lateral resolution of 100-120 nm, we investigated the basal-level spatial distributions of the four major types of endocytic pits across distinct neuronal compartments, including the AIS, distal axons, soma, and dendrites. To accurately distinguish these neuronal compartments, we used neurofascin, tau, and MAP2 as markers for the AIS, distal axonal segments, and dendrites, respectively (**Fig. 1A-D and Fig. S2C-F**). We quantified basal-level densities of these endocytic pits using endocytic pit area fraction, defined as the ratio of total endocytic pit area to the corresponding compartmental area demarcated by these markers. We found that all four types of endocytic pits were present in all neuronal compartments examined. CCPs

and Flot1-pits were denser in distal axons than in any other neuronal compartments, whereas Cav1- and EndoA2-pits were denser in dendrites compared to other neuronal compartments (**Fig. 1E**), indicating that these four endocytic pathways are differentially regulated across distinct neuronal compartments.

Having established the basal-level distributions of these endocytic pits across different neuronal compartments, we next aimed to examine the regulatory role of the MPS in modulating these distributions. To study how MPS disruption affects the basal-level distributions and densities of the four types of endocytic pits, we transduced neurons with adenovirus expressing short hairpin RNA (shRNA) against βII-spectrin, a key structural component of the MPS, to disrupt the MPS both in the axonal and somatodendritic compartments, as described previously(*15, 18, 23, 27*). The βII-spectrin expression level in βII-spectrin knockdown (KD) neurons decreased by ~70%, compared to wild-type (WT) neurons, which were transduced with adenovirus expressing scrambled control shRNA as a control (**Fig. S2A-B**). The immunostained patterns for endogenous CCPs, Cav1-pits, Flot1-pits, and EndoA2-pits in mature (DIV 21-28) WT and βII-spectrin KD neurons showed that MPS disruption significantly increased the densities of all four types of endocytic pits in all neuronal compartments examined including AIS, distal axonal segments, and dendrites, compared to WT neurons (**Fig. S2G-H and Fig. 1F-I**). To determine whether such enhancement of endocytosis observed in mature βII-spectrin KD neurons reflected MPS disruption rather than MPS-independent effects of βII-spectrin depletion, we analyzed younger neurons (DIV7), a developmental stage at which the dendritic MPS is not yet established(*18*). In these immature neurons, endocytic pit densities were comparable between WT and βII-spectrin KD neurons, suggesting that the enhanced pit densities observed in mature βII-spectrin KD neurons are likely due to MPS disruption rather than other MPS-independent effects (**Fig. S2I-J**). Together, these results suggest that the MPS functions as a physical barrier to suppress basal endocytosis across all four endocytic pathways in all neuronal compartments, likely by acting as a physical barrier that restricts endocytic pit formation.

Four major types of endocytic pits are localized within "clearings" of the MPS lattice in axons

We further investigated the structural basis underlying the MPS's inhibitory role in regulating four major types of endocytosis in axons. To resolve the spatial relationship between endocytic pits and the MPS, we employed dual-color three-dimensional (3D) stochastic optical reconstruction microscopy (STORM)(*36, 38*), a super-resolution imaging technique with lateral resolution of 20–30 nm and axial resolution of 50–60 nm (**Fig. 2A**). The MPS was visualized in cultured mature neurons (at or after DIV 21) through immunostaining of the C-terminus of βII-spectrin or adducin, which mark the periodic "rings" formed by spectrin tetramer centers or actin filaments, respectively. Endocytic pits were immunostained using either antibodies against endogenous endocytic proteins, or an anti-GFP antibody for labeling the exogenously expressed GFP-tagged endocytic proteins through low-titer lentiviral transduction.

3D STORM cross-sections (*y/z* views) revealed that all four types of endocytic pits were present both at the plasma membrane and within axonal shafts (**Fig. S3A**), with the fractions of endogenous endocytic pits being localized at the cell surface being 78.9 ± 4.0%, 82.3 ± 1.8%, 67.2 ± 1.7% and 67.0 ± 6.9% for CCPs, Cav1-pits, Flot1-pits, and EndoA2-pits, respectively (**Fig. S3B**). The surface-localized fractions of GFP-tagged endocytic pits closely resembled those of their endogenous counterparts, except for GFP-tagged Cav1 pits, which displayed a slightly lower surface-localized fraction, suggesting that both labeling strategies yield comparable results. To further validate our quantification method, we treated neurons with dyngo-4a, a potent dynamin inhibitor that prevents CCP scission from the plasma membrane(*39*) , which led to an expected increase in the fraction of surface-localized CCPs in both axonal and dendritic compartments, confirming the reliability of our measurements (**Fig. S3D**).

Next, we quantified the diameters of all four types of endogenous endocytic pits localized at the plasma membrane, which averaged 82.5 ± 2.8, 75.0 ± 4.3, 71.7 ± 2.8 and 67.0 ± 3.4 nm for CCPs, Cav1-pits, Flot1-pits, and EndoA2-pits, respectively (**Fig. S3C**). The average diameters for the internalized fractions of the four endogenous endocytic pits were similar to those of surface-localized pits, indicating that the majority of surface-localized puncta analyzed are likely fully assembled endocytic pits (**Fig. S3C, E**). In addition, GFP-tagged endocytic pits exhibited similar diameters to their endogenous counterparts, for both surface-localized and internalized fractions (**Fig. S3C**).

For the surface-localized fractions of these four types of endocytic pits, we examined their spatial distributions relative to the MPS in axons by classifying the relative positions of endocytic pits into two scenarios (**Fig. 2B-C**): Class I) The pit has no overlap with the MPS; and Class II) the pit overlaps with the MPS. Quantification revealed that Class I pits were much more prevalent than Class II pits for all four types of endocytic pits, suggesting that all four types of pits are spatially excluded from the MPS (**Fig. 2D, G, J, M, P**). To confirm this exclusion, we calculated the Pearson's correlation coefficients between the surface-localized pits and the MPS across 70-130 axonal regions, and found that these experimental coefficient values were significantly lower than those calculated from randomization controls, where the positions of all pits in each analyzed axonal region were randomly shuffled before calculating the Pearson's correlation coefficient (**Fig. 2E, H, K, N**). As negative controls, we labeled neurons with two widely used membrane markers wheat germ agglutinin (WGA) and cholera toxin B subunit (CTB), and imaged their spatial distributions relative to the MPS in axons using STORM, following the same procedure as for the endocytic pits. The calculated Pearson's correlation coefficients between either membrane marker and the MPS were not significantly different from those calculated from randomized controls, supporting the observed spatial exclusion between pits and the MPS as a true biological pattern (**Fig. S4A-D**). In addition, we compared the quantification results obtained from endogenously labeled pit

proteins with those obtained from exogenously expressed GFP-tagged pit proteins (**Fig. S5A-G)**. Both labeling strategies yielded comparable results. Finally, to better visualize the average spatial pattern of these exclusion zones, we generated averaged dual-color STORM images by aligning individual cropped images centered on each endocytic pits, without reorienting neurites to the same MPS periodic axis. For all four types of pits, the corresponding radial fluorescence intensity profiles revealed that these pits are located in regions devoid of MPS immunostaining (**Fig. 2F, I, L, O**). These circular "clearing" structures observed closely resembled those CCP-centered "clearings" previously observed at the AIS(*30*). It is worth noting that these MPS-surrounding circular "clearings" in the averaged dual-color STORM images were consistently observed regardless of the MPS labeling strategy(**Fig. S4E-K**), whether visualized via the C-terminal of βII-spectrin (marking spectrin tetramer centers) or adducin (marking spectrin tetramer ends), indicating that endocytic pits are excluded from the entire MPS-occupied membrane region. Together, these findings demonstrate that CCP-centered clearings are not only present at or near the AIS but also extend into distal axonal segments, and similar clearings are also present in the axons for the three clathrin-independent endocytic pits examined.

Four major types of endocytic pits are localized within "clearings" of the MPS lattice in dendrites

The initial "clearing" study reported that CCP-centered "clearings" observed at the AIS were absent from somatodendritic compartments(*30*). However, this absence may be attributed to imaging being performed on DIV14 neurons, while the MPS develops much more slowly in somatodendrites than in axons(*18*). The MPS coverage across the plasma membrane of somatodendrites reaches only ~50% saturation around DIV 21–28, whereas MPS coverage in axons reaches ~90% by DIV 14. This developmental delay raises the possibility that similar clearings may emerge in somatodendrites of more mature neurons (DIV 21 or older).

Since the MPS coverage is comparable between the soma and dendrites in mature neurons, and STORM imaging is technically easier in dendrites, we selected dendrites as the representative somatodendritic compartment for our imaging analysis (**Fig. 3A**). We first examined the spatial relationship between each of the four endocytic pit types and the surface-localized MPS in the radial direction within cross-section images of dendrites. The dendritic MPS was labeled by immunostaining either adducin or the N-terminus of βIII-spectrin (a β-spectrin isoform present primarily in somatodendrites but not axons), both of which mark the periodic "rings" formed by actin filaments (**Fig. 3B)**. Endocytic pits were immunostained using the same two labeling strategies employed for axon imaging. 3D STORM cross-sections (y/z views) revealed that all four types of endocytic pits were present both at the plasma membrane and within dendritic shafts (**Fig. S3F**), with the surface-localized fractions being similar to those observed in axons (**Fig. S3G**). The average diameters of the internalized endocytic pits closely matched those of the surface-

localized fractions, and these average diameters determined in dendrites were comparable to those observed in axons. Both labeling strategies for endocytic pits produced consistent results (**Fig. S3H**).

We then examined the spatial relationship between each type of endocytic pit and the MPS in top-view STORM images of dendrites. As in the axon analysis, endocytic pits were classified into two classes based on their spatial overlap with the MPS. Two-color STORM revealed that Class I pits (i.e., pits without overlap with the MPS) were markedly more prevalent than Class II pits for all four types of endocytic pits (**Fig. 3C, F, I, L, O and Fig. S5H, J, L, N**). The spatial exclusion pattern of endocytic pits from the MPS was confirmed by Pearson's correlation analysis as performed for axons, where the experimental coefficients calculated from experimental images were significantly lower than those calculated from the corresponding randomization controls (**Fig. 3D, G, J, M and Fig. S5I, K, M**). Finally, intensity profiles from averaged STORM images aligned to the centers of endocytic pits revealed circular "clearings" surrounding clathrin-, Cav1-, Flot1- or EndoA2-endocytic pits in dendritic compartments (**Fig. 3E, H, K, N**). Together, these results suggest that circular "clearings" are a conserved structure in both axonal and somatodendritic compartments of mature neurons, with both clathrin-dependent and clathrin-independent endocytic pits residing at their centers.

MPS inhibits ligand-induced endocytosis in both axonal and somatodendritic compartments

Given our observation that MPS disruption significantly increased the basal endocytosis of the four major types across all neuronal compartments, we investigated whether the MPS similarly inhibits ligand-induced endocytosis mediated by clathrin, caveolin, flotillin, or endophilin – which are generally considered to occur more rapidly than basal-level, constitutive endocytosis.

We first examined transferrin and low-density lipoprotein (LDL) endocytosis in neurons, both of which are forms of ligand-induced endocytosis primarily mediated by clathrin (i.e., CME) in most cell types(*40, 41*). Incubating fluorophore-conjugated transferrin or LDL with cultured neurons resulted in an increased number of internalized transferrin or LDL over time in the somatodendrites but not axons, consistent with previous studies(*40, 41*). To ensure that only internalized ligands were quantified, we performed an acid wash to remove surface-bound transferrin or LDL before imaging. To further validate the endocytic pathways involved in transferrin or LDL uptake, we pretreated neurons with four inhibitors targeting distinct pathways(*1*) and assessed their effects, including: 1) shRNA against clathrin heavy chain (CHC) to disrupt CME(*42*) with CHC knockdown confirmed by more than a 60% reduction of CHC immunofluorescence intensity in CHC KD neurons compared to WT neurons (**Fig. S6A, B**); 2) dyngo-4a, which inhibits CME, FEME and certain types of LRME; 3) nystatin, which disrupts lipid rafts and hence LRME by sequestering cholesterol; and 4) 5-[N-ethyl-N-isopropyl] amiloride (EIPA), a

Na^+/H^+ exchanger inhibitor that disrupts macropinocytosis but not receptor-mediated endocytosis. Transferrin uptake by neurons was inhibited by CHC knockdown, dyngo-4a and EIPA but not by nystatin (**Fig. S6C, D**), suggesting that transferrin uptake depends on CME and possibly macropinocytosis. Consistent with this, imaging revealed that internalized transferrin strongly colocalized with clathrin but not with Cav1, Flot1, or EndoA2 (**Fig. S6E, F**), further supporting CME as the primary pathway of transferrin uptake. In contrast, LDL uptake was inhibited only by CHC knockdown and dyngo-4a, indicating that LDL uptake relies exclusively on CME (**Fig. S6I, J**). To determine whether MPS disruption affects clathrin-mediated transferrin and LDL uptake, we quantified the area fraction of internalized transferrin or LDL puncta, defined as the ratio of total transferrin or LDL puncta area to the corresponding dendritic area, in both WT and βII-spectrin KD neurons (**Fig. 4A and Fig. S6K**). By fitting the puncta area fraction over time to a single-exponential curve, we determined the time constants for uptake. Such time-course analysis revealed that transferrin uptake was faster in βII-spectrin KD neurons with a time constant $\tau = 8.29 \pm 0.37$ min, compared to $\tau = 17.15 \pm 0.89$ min in WT neurons (**Fig. 4B)**. Similarly, LDL uptake was enhanced in βII-spectrin KD neurons ($\tau = 35.25 \pm 1.49$ min), compared to WT neurons ($\tau = 54.63 \pm 2.45$ min) (**Fig. S6L)**. Notably, βII-spectrin knockdown did not alter surface expression levels of transferrin receptors or LDL receptors, ruling out increased surface expression levels of transferrin receptors or LDL receptors as a cause for the accelerated transferrin or LDL-induced endocytosis (**Fig. S6G, H, M, N**). Together, these findings indicate that the MPS acts as a physical barrier to restrict ligand-induced CME.

We next examined whether MPS disruption affects ligand-induced LRME. A previous study reported that in cultured neurons overexpressing HA-tagged metabotropic glutamate receptor 5a with the HA epitope tag located on its extracellular N-terminus (HA-mGluR5a), treatment with an anti-HA antibody induced HA-mGluR5a endocytosis across all neuronal compartments via a proposed lipid raft-mediated and clathrin-independent pathway(*43*). Using the same assay, treatment with the anti-HA antibody followed by an acid wash to remove surface-bound antibody resulted in a punctate immunostaining pattern of HA-mGluR5a, indicating its internalization. A subset of these puncta was colocalized with Cav1 pits but not with clathrin-, Flot1-, or EndoA2- pits (**Fig. S7A, B**), supporting a caveolin-mediated mechanism. To confirm the endocytic pathway involved, we tested the effects of the four inhibitors described above. Antibody-induced HA-mGluR5a endocytosis was significantly inhibited by dyngo-4a or nystatin, but not by CHC knockdown or EIPA, further indicating that HA-mGluR5a endocytosis occurs, at least partially, through caveolin-mediated endocytosis, a major LRME pathway (**Fig. S7C, D**). Next, we assessed the effect of MPS disruption on antibody-induced HA-mGluR5a endocytosis. WT and βII-spectrin KD neurons were incubated with the anti-HA antibody over a time course, followed by immunostaining for internalized HA-mGluR5a and endogenous Cav1. This allowed us to selectively analyze the fraction of

internalized HA-mGluR5a that colocalized with endogenous Cav1-pitsa (**Fig. 4C**). Time-course analysis revealed that caveolin-mediated HA-mGluR5a endocytosis occurred faster in βII-spectrin KD neurons ($\tau = 9.18 \pm 0.68$ min) compared to WT neurons ($\tau = 37.77 \pm 4.24$ min) (**Fig. 4D**). This enhancement was not due to changes in the surface expression of HA-mGluR5a (**Fig. S7E, F**). Together, our data indicates that MPS disruption facilitates ligand-induced LRME.

Finally, we assessed the impact of MPS disruption on ligand-induced FEME. When examining endogenous neural cell adhesion molecule 1 (NCAM1) internalization in mature neurons, triggered by treatment with a monoclonal anti-NCAM1 antibody against its extracellular domain, we found that the internalized NCAM1 puncta colocalized with EndoA2-pits but not with clathrin-, Cav1-, or Flot1-pits (**Fig. S7G, H**). Inhibitor experiments revealed that antibody-induced NCAM1 endocytosis was inhibited only by dyngo-4a, with no effect observed from CHC knockdown, nystatin, or EIPA (**Fig. S7I, J**). These results indicate that NCAM1 endocytosis occurs, at least partially, through endophilin-mediated endocytosis (i.e., FEME) in neurons. To assess the effect of MPS disruption, we compared the time course of NCAM1 endocytosis, specifically only for the fraction of NCAM1 puncta colocalized with endogenous EndoA2-pits, in WT and βII-spectrin KD neurons (**Fig. 4E**). Since βII-spectrin KD neurons exhibited ~10% higher NCAM1 surface expression (**Fig. S7K, L)**, we selected neurite regions from both groups with comparable NCAM1 surface levels for our time course analysis. Our results showed that the internalization of the NCAM1 pool that is mediated by EndoA2 was increased in both axonal and dendritic compartments of βII-spectrin KD neurons compared to WT neurons (**Fig. 4F**), demonstrating that the MPS also restricts ligand-induced FEME. Together, our findings demonstrate that the MPS serves as a regulatory barrier that inhibits both clathrin-dependent and clathrin-independent ligand-induced endocytosis in axonal and somatodendritic compartments.

The MPS acts as a dynamic barrier modulated by endocytosis and ERK signaling through a positive feedback mechanism

We next investigated whether ligand-induced endocytosis can, in turn, affect the MPS. Previously, we demonstrated that ligand binding to the extracellular domain of cannabinoid type 1 receptor (CB1) or NCAM1 induces the activation of the extracellular signal–regulated kinase (ERK) (*23*), a key cell signaling pathway that involved in neuronal development and stress response, and hippocampal learning and survival(*44*). While we observed that CB1 ligand-induced ERK activation resulted in calpain-dependent MPS degradation(*23*), it remains unclear whether this phenomenon is common across other ligand-receptor systems (**Fig. 5A**). Using an IF-based ERK activation assay previously developed to monitor CB1- and NCAM1-induced ERK activation(*23*) , we quantitatively assessed phosphorylated ERK (pERK) levels at different time points after ligand stimulation of three receptors: transferrin receptor

(TfR), HA-tagged mGluR5a, and NCAM1. All ligand treatments induced ERK activation, which persisted for up to 60 minutes post-treatment (**Fig. 5B, C**). Inhibiting ligand-induced TfR, HA-mGluR5a and NCAM1 endocytosis using dyngo-4a significantly reduced ERK activation (**Fig. 5B, C)**, indicating that a substantial portion of ERK activation occurs at internalized endosomes, and that ligand-induced endocytosis of TfR, mGluR5a and NCAM1 effectively contributes to ERK signaling. Notably, this contrasts with CB1 ligand-induced ERK activation, which does not rely on CB1 endocytosis and instead appears to occur primarily at the cell surface rather than in endosomes(*23*).

We next investigated whether ligand-induced endocytosis and ERK activation leads to protease-dependent MPS degradation. Using average 1D autocorrelation amplitude analysis, a quantification method we previously developed to measure the integrity of MPS(*23*), we examined the effects of ligand-induced TfR, HA-mGluR5a, or NCAM1 endocytosis on MPS structure in neurons. Quantitative analysis of 3D STROM images of βIII-spectrin revealed significant MPS degradation following ligand stimulation, as evidenced by decreased average 1D autocorrelation amplitudes (**Fig. 5D, E**). Inhibiting ligand-induced TfR, HA-mGluR5a, or NCAM1 endocytosis using dyngo-4a prevented MPS degradation (**Fig. 5D, E)**. Preincubation with U0126, an inhibitor of MEK, the kinase upstream of ERK, also protected the MPS from degradation (**Fig. 5D, E)**. These results indicate that both endocytosis and ERK activation are upstream events required for MPS degradation. To identify the proteases involved, we tested the effects of MDL-28170 (MDL; a calpain inhibitor) and Z-VAD-FMK (VAD; a caspase inhibitor), both of which are known to cleave brain spectrin(*45*) and can be activated by ERK(*46, 47*). Treatment of neurons with either protease inhibitor rescued MPS integrity, with varying degrees of protection, suggesting that endocytosis-induced MPS degradation is calpain- and caspase-dependent (**Fig. 5D, E**).

To further confirm protease-mediated MPS degradation, we examined the characteristic proteolytic profiles of αII- and βII-spectrin breakdown products using western blotting. Previous studies have well documented that calpain- and caspase-mediated spectrin cleavage yield distinct proteolytic fragments detectable by western blot: for αII-spectrin, calpain generates a major 150 kDa fragment, whereas caspase produces a 120 kDa fragment; for βII-spectrin, calpain generates 110 kDa and 85 kDa fragments, whereas caspase produces 108 kDa and 80 kDa fragments(*45*). Following ligand-induced endocytosis of TfR, NCAM1 or HA-mGluR5a, the 280 kDa full length αII-spectrin was primarily cleaved into the 150 kDa fragment, with only a faint 120 kDa fragment observed (**Fig. S8A, B**), indicating that calpain is the primary protease responsible for endocytosis-induced MPS degradation. Pretreating neurons with MDL markedly reduced the 150 kDa band, confirming its calpain specificity. Pretreatment with VAD modestly attenuated the 150 kDa band, likely reflecting VAD's known partial inhibition of calpain(*48*). For the 260 kDa full-length βII-spectrin, analysis of its breakdown products yielded results consistent with αII-

spectrin, although the calpain-derived (110/85 kDa) and caspase-derived (108/80 kDa) fragments could not be clearly distinguished due to their close molecular weights (**Fig. S8A, B**). Collectively, these results indicate that ligand-induced MPS degradation occurs primarily via calpain-mediated spectrin cleavage, with minimal contribution from caspase activity.

To further probe whether increased endocytosis alone could degrade the MPS, we investigated whether moderate overexpression of GFP-tagged endocytic pit proteins (i.e., Cav1, Flot1, and EndoA2) which may increase endocytic pit density, could similarly affect MPS integrity. We first confirmed that overexpressing these endocytic pit proteins in neurons significantly increased the endocytic pit area fractions compared to WT neurons, as quantified from the 3D STORM images described above (**Fig. S9A**). We then assessed MPS integrity using epi-fluorescence and STORM imaging. Compared to WT neurons and neurons overexpressing a plasma membrane-associated protein BSAP1 (an endocytic pit-irrelevant control), neurons overexpressing GFP-tagged Cav1, Flot1, or EndoA2 exhibited a moderate decrease in both the average βII-spectrin immunofluorescence intensity (quantified by epi-fluorescence imaging) and the average 1D autocorrelation amplitude (quantified by STORM imaging) in axons and dendrites (**Fig. S9B-E**). These findings suggest that increased endocytic pit density and enhanced endocytosis activity alone can induce moderate MPS degradation, further supporting our model that endocytosis contributes to MPS disruption.

So far, our data demonstrates that the MPS suppresses endocytosis and conversely, endocytosis can lead to MPS degradation. This reciprocal relationship suggests that endocytosis-induced MPS degradation may be a programmed cellular mechanism designed to rapidly remove the MPS barrier, facilitating accelerated endocytosis once triggered. To further test this hypothesis, we examined whether preventing MPS degradation could suppress ligand-induced endocytosis. For both ligand-induced TfR and HA-mGluR5a endocytosis, we quantified the internalized endocytic pit area fractions following ligand treatment, with or without calpain or caspase inhibitor treatment. Neurons were treated with either protease inhibitor, both prior to ligand addition and continuously throughout the endocytosis process. Compared to untreated conditions, inhibiting MPS degradation via calpain or caspase inhibitors significantly reduced ligand-induced TfR and HA-mGluR5a endocytosis (**Fig. 5F-I**). These results support our model that the MPS acts as a dynamic physical barrier to suppress endocytosis. When rapid endocytosis is required, cells activate ERK-protease pathways to induce calpain- and/or caspase-dependent MPS degradation, thereby removing the MPS barrier and promoting faster receptor internalization. This mechanism establishes a previously unknown positive feedback loop, wherein endocytosis drives MPS degradation, which in turn accelerates subsequent endocytosis and amplifies downstream signaling to support rapid neuronal responses (**Fig. 5J**).

The MPS serves as a neuroprotective barrier by restricting APP endocytosis and Aβ42 accumulation

Increasing evidence indicates that dysregulated endocytosis in neurons contributes to the pathogenesis of Alzheimer's disease (AD), a progressive neurodegenerative disorder where dementia symptoms gradually worsen over a number of years(*3, 4*). Elevated production and accumulation of misfolded β-amyloid peptide (Aβ) in the brain correlates with neuronal aging and the AD development. The pathogenic form of Aβ (Aβ42) is generated from amyloid precursor protein (APP) after cell surface-localized APP undergoes endocytosis and is processed by sequential β- and γ-secretase cleavage in neuronal endosomes and lysosomes(*49*) (**Fig. 6A**). This raises the possibility that the MPS may have a neuroprotective role by suppressing APP endocytosis, thereby limiting Aβ production and accumulation.

To test this hypothesis, we employed a previously established ligand-induced APP endocytosis system(*50*) to manipulate and monitor APP endocytosis in neurons. In this system, a GFP variant, super-ecliptic pHluorin (SEP), was fused to the N-terminus of APP695, the predominant APP isoform in neuronal tissues (**Fig. 6B**). Treating neurons overexpressing SEP-APP with a fluorophore-conjugated nanobody (~ 15 kDa) against SEP induced SEP-APP endocytosis in the somatodendritic compartments(*50*). Pretreating neurons with our four described inhibitors revealed that SEP-APP endocytosis involves complex pathways, proceeding through both clathrin-dependent and clathrin-independent pathways (**Fig. S10A, B**). This finding contrasts with a previous study that identified nanobody-induced SEP-APP endocytosis as strictly clathrin-independent(*50*), potentially due to differences in experimental conditions. We then compared SEP-APP endocytosis rates in both WT and βII-spectrin KD neurons. SEP-APP uptake was significantly faster in βII-spectrin KD neurons ($\tau = 14.52 \pm 0.38$ min) compared to WT neurons ($\tau = 37.21 \pm 5.11$ min), suggesting that MPS degradation accelerated APP internalization (**Fig. S10C, D**). Notably, this endocytosis enhancement was not due to an increased APP surface or total expression upon βII-spectrin knockdown (**Fig. S10E-H**). Similar to other ligand-induced endocytosis observed in this study, SEP-APP endocytosis activated sustained downstream ERK signaling, as indicated by increased pERK immunofluorescence (**Fig. 6C, D**). Following the nanobody-induced SEP-APP endocytosis, significant MPS degradation was observed, shown by reduced 1D autocorrelation amplitude of the periodic βIII-spectrin distribution (**Fig. 6E, F**). Inhibiting SEP-APP endocytosis using dyngo-4a or U0126 prevented MPS degradation, indicating the MPS degradation is endocytosis- and ERK-dependent. Moreover, this MPS degradation was partially prevented by calpain or caspase inhibitor treatment, indicating that MPS degradation was mediated by calpain- and caspase-dependent spectrin cleavage (**Fig. 6E, F**). Western blot analysis of the proteolytic profiles of αII- and βII-spectrin breakdown products indicated the primary protease responsible for APP-endocytosis induced MPS degradation is calpain (**Fig. S8C**). Conversely,

protecting MPS from degradation using calpain or caspase inhibitor significantly reduced SEP-APP endocytosis in neurons (**Fig. 6G, H**), reinforcing the role of the MPS as a regulatory barrier that restricts APP internalization. These findings suggested that APP endocytosis promotes ERK signaling, which facilitates MPS degradation, establishing a positive feedback loop that accelerates APP internalization.

We next examined whether increased APP endocytosis in MPS-disrupted neurons leads to elevated Aβ production, a hallmark of AD. To avoid potential confounding effects from SEP tagging, we quantified the Aβ accumulation in cultured mature neurons with and without overexpressing wild-type APP695 (APPwt) or APP695 bearing the K670M/N671L Swedish mutation (APPswe), a familial AD-associated variant known to enhance Aβ accumulation. We employed a previously developed IF-based Aβ42 quantification assay using a highly specific anti-Aβ42 C-terminal antibody(*51*). Immunostaining of intracellular Aβ42, the key pathogenic form of Aβ, revealed elevated Aβ42 levels in neurons overexpressing either APPwt or APPswe, compared to neurons without APP overexpression (i.e., WT neurons), confirming that overexpressing APPwt and APPswe lead to increased intracellular Aβ42 production(*52*) (**Fig. 6I-J)**. Interestingly, βII-spectrin KD neurons overexpressing APPwt or APPswe exhibited significantly higher levels of intracellular Aβ42 accumulation than WT neurons overexpressing APPwt or APPswe (**Fig. 6I-J)**. It is important to note that Aβ42 levels remained comparable between WT and βII-spectrin KD neurons without APP overexpression, indicating that the observed increase in Aβ42 accumulation requires both MPS disruption and APP overexpression. Together, these findings suggest that the MPS plays a neuroprotective role in limiting Aβ42 accumulation, likely by suppressing APP endocytosis and reducing subsequent secretase-mediated APP cleavage in endosomes and lysosomes of neurons.

Intraneuronal Aβ42 accumulation occurs before the formation of extracellular Aβ plaques and is known to trigger a cascade of pathological events, including proteasome and mitochondrial dysfunction, calcium dysregulation, and synaptic impairment(*53*). Since intraneuronal Aβ42 accumulation has been previously linked to activation of caspase-3, a canonical marker of apoptosis, as well as neuronal apoptosis(*52, 54*), we investigated whether MPS disruption exacerbates Aβ42-mediated neurotoxicity by comparing caspase-3 activations levels in WT and βII-spectrin KD neurons with and without APPwt or APPswe overexpression. Immunostaining for cleaved (activated) caspase-3 using a previously reported, highly specific anti-caspase-3 antibody(*29*) revealed significantly higher caspase-3 activation in neurons overexpressing APPwt or APPswe compared to non-overexpressing controls, with even greater caspase-3 activation observed in βII-spectrin KD neurons (**Fig. 6K-L**), supporting the hypothesis that MPS disruption accelerates APP internalization and subsequent Aβ42 production, thereby promoting neurotoxicity and neuronal apoptosis. Importantly, the observed patterns of caspase-3 activation mirrored

the corresponding Aβ42 accumulation levels across WT and βII-spectrin KD neurons with and without APP overexpression, suggesting that elevated apoptosis signals are likely a direct consequence of increased Aβ42 accumulation. Together, these findings support a model in which the MPS acts as a neuroprotective barrier that restricts APP endocytosis, thereby limiting intraneuronal Aβ42 production, accumulation and subsequent neuronal apoptosis (**Fig. 6M**). When the MPS degradation occurs, previously observed in both aged and the neurodegenerative conditions(*55*), APP endocytosis accelerates, leading to pathological Aβ42 accumulation, neuronal dysfunction, and ultimately neuronal death. This mechanism provides insight into how MPS degradation may contribute to the progression of Alzheimer's disease, and highlights preserving MPS integrity as a potential therapeutic strategy to mitigate APP-related neurodegeneration.

Discussion

In this study, we leveraged super-resolution fluorescence imaging to visualize the structural interplay between the MPS and endocytic events at nanoscale resolution, and identified endocytic "clearing" structures analogous to those previously reported for CCPs at the AIS and proximal axon(*30*). Notably, we extended these observations to distal axonal and somatodendritic compartments, which were not reported in the initial study(*30*). The absence of such structures in the initial study may be due to the use of immature neurons, in which the somatodendritic MPS had not yet developed into a sufficiently dense and continuous lattice network(*18*). Importantly, we found that these clearing structures are not unique to CME but also observed for other major endocytic pathways, including LRME, such as caveolin- and flotillin-mediated internalization, as well as FEME. These findings reveal that MPS-based clearings represent a conserved structural feature across multiple endocytic mechanisms. Our super-resolution imaging thus provides direct structural evidence that the MPS functions as a spatial gatekeeper of endocytosis, regulating access through discrete clearings embedded within the periodic actin-spectrin lattice.

Aligned with our structural findings, functional assays comparing the endocytosis rates in neurons with and without MPS disruption support the role of the MPS as a universal regulator of all major endocytic pathways, including CME, LRME, and FEME. Disruption of the MPS not only resulted in a pronounced elevation of the intrinsic, basal-level endocytic activity across multiple pathways, but also markedly accelerated ligand-induced internalization events mediated through CME, LRME, and FEME, underscoring the MPS's central role as a structural suppressor of both constitutive and stimulus-evoked endocytic processes. Importantly, our data reveals that ligand-induced endocytosis itself activates a positive feedback loop that further accelerates endocytic uptake: ligand-induced endocytosis triggers sustained ERK activation, which in turn activates calpain and caspase to cleave spectrin and degrade the

MPS; This degradation process effectively removes the MPS-imposed barrier, thereby facilitating faster and more robust endocytic uptake. The presence of this positive feedback loop illustrates a finely tuned mechanism whereby neurons can rapidly enhance endocytosis when rapid signaling or cargo internalization is required. This dynamic interplay underscores the MPS as both a gatekeeper and a responsive element in endocytic regulation.

In addition to CME, our findings reveal that other major endocytic pathways, including LRME and FEME, also occur at the AIS, distal axon, and somatodendritic compartments of neurons under basal (unstimulated) conditions. This broad spatial distribution underscores the pervasive and compartmentally integrated nature of endocytosis in mature neurons, extending beyond the traditionally emphasized role of CME. By using a panel of well-characterized ligands and assessing their colocalization with pathway-specific endocytic structures, we were able to selectively probe the activity of distinct endocytic mechanisms: transferrin and LDL for CME, mGluR5a for LRME, and NCAM1 for FEME. These assays provide a robust framework for the investigation of specific endocytic pathways in neurons.

Our findings also reveal important implications for neuronal health and disease. We observed that MPS degradation accelerates APP endocytosis, leading to increased production and intracellular accumulation of Aβ42, a pathogenic hallmark of Alzheimer's disease. The elevated intraneural Aβ42 levels resulting from increased APP internalization were accompanied by downstream neurotoxic events, such as increased activation of caspase-3, which has been observed in Alzheimer's brain(*56*). Stabilizing the MPS using calpain or caspase inhibitors reduced APP endocytosis, suggesting that the MPS serves as a neuroprotective structure that restricts excessive APP internalization and potentially slows down subsequent Aβ42 generation and caspase-3 activation. Moreover, the positive feedback loop we identified—whereby endocytosis triggers ERK activation, leading to protease-mediated MPS degradation—provides a plausible mechanism through which neurodegeneration may be exacerbated. Supporting this idea, spectrin cleavage products have been proposed as biomarkers for aging and neurodegenerative diseases(*57*). In aging neurons or those subjected to chronic stress, MPS instability may initiate a self-perpetuating cycle of heightened endocytosis and sustained ERK signaling, further accelerating APP internalization and Aβ42 accumulation. This insight is consistent with growing evidence that dysregulated endocytosis and protease activation contribute to Alzheimer's pathogenesis.

Together, these findings position the MPS as a central structural regulator of neuronal endocytosis, capable of both constraining and dynamically modulating membrane trafficking across diverse cellular contexts. By uncovering its roles in both physiological regulation and disease-relevant pathways, our study not only expands the conceptual framework of endocytic control in neurons but also highlights the MPS as a potential therapeutic target for modulating endocytosis in neurodegenerative disorders.

Materials and Methods

Primary culture of mouse hippocampal neurons

All experimental procedures were conducted in accordance with the Guide for the Care and Use of Laboratory Animals of the National Institutes of Health. The protocol (PROTO202101857) was approved by the Institutional Animal Care and Use Committee (IACUC) of the Pennsylvania State University. Primary cultures of hippocampal neurons were prepared as previously described(*18*). Briefly, timed-pregnant CD-1 IGS mice (Charles River Laboratories, Wilmington, MA; 022) were euthanized, and hippocampi were isolated from E18 mouse embryos. The dissected tissues were enzymatically dissociated with 0.25% trypsin-EDTA (1x) (Sigma, T4549) at 37 °C for 15 minutes. Following digestion, the hippocampal tissues were washed three times with Hanks' Balanced Salt Solution (HBSS) (Thermo Fisher Scientific, 14175095), and then transferred to NbActiv1 culture medium (Transnetyx, NB1500 ml), a pre-mixed formulation comprising Neurobasal, B27, and Glutamax, with the addition of 100 μg/ml Primocin (InvivoGen, ant-pm-2). The tissues were gently triturated in the culture medium until a single-cell suspension was achieved, ensuring no tissue clumps remained. Dissociated cells were then counted and plated onto poly-D-lysine-coated 18-mm coverslips (Neuvitro, GG-18-1.5-PDL). Cultures were maintained in a humidified incubator at 37□°C with 5% CO□. Half of the medium volume was replaced every five days to maintain optimal culture conditions. Unless otherwise specified, neurons were fixed between 21 and 28 days in vitro for subsequent experiments described in this study.

Antibodies

The following primary antibodies were used in this study: guinea pig anti-tau antibody 1:500 dilution for immunofluorescence (IF) (Synaptic Systems, 314004), mouse anti-tau antibody 1:500 dilution for IF (BD Biosciences, 556319), guinea pig anti-MAP2 antibody 1:500 dilution for IF (Synaptic Systems, 188004), rabbit anti-MAP2 antibody 1:500 dilution for IF (Synaptic Systems, 188002), chicken anti-neurofascin antibody (R&D system, AF3235), rabbit anti-clathrin heavy chain antibody 1:500 dilution for IF (Abcam, ab21679), rabbit anti-caveolin-1 antibody 1:400 dilution for IF (Cell signaling, 3238S), mouse anti-flotillin-1 antibody 1:100 dilution for IF (BD Biosciences, 610820), mouse anti-endophilinA2 antibody 1:100 dilution for IF (Santa Cruz, sc-365704), mouse anti-αII-spectrin (EnCor Biotechnology, MCA-3D7), mouse anti-βII spectrin antibody 1:200 dilution for IF (Santa Cruz, sc-515592), mouse anti-βII spectrin antibody 1:200 dilution for IF (BD Biosciences, 612563), rabbit anti-adducin antibody 1:500 dilution for IF (Abcam, ab51130), chicken anti-GFP antibody 1:500 dilution for IF (Thermo Fisher Scientific, A10262), rabbit anti-GFP antibody 1:500 dilution for IF (Thermo Fisher, A11122), goat anti-βIII spectrin antibody 1:100 dilution for IF (Santa Cruz, sc-9660), mouse anti-βIII spectrin antibody 1:100

dilution for IF (Santa Cruz, sc-515737), mouse anti-HA antibody 1:200 dilution for HA-mGluR5a internalization and IF (Thermo Fisher Scientific, 26183), rat anti-NCAM1 (CD56) antibody 1:40 dilution for NCAM1 internalization and IF (Cedarlane, CL10008AP), rat anti-TfR (CD71) antibody 1:500 dilution for IF (Bio-Rad, MCA1033GA), goat anti-LDLR antibody 1:100 dilution for IF (Thermo Fisher Scientific, PA5-46987), rabbit anti-phospho-ERK antibody 1:300 dilution (Cell Signaling Technology, 4370S), mouse anti-Aβ42 antibody 1:200 dilution for IF (Biolegend, 805501), rabbit anti-cleaved caspase-3 (Asp175) antibody 1:400 dilution for IF (Cell Signaling Technology, 9661).

The following secondary antibodies were used in this study: Alexa Fluor-647-conjugated donkey anti-guinea pig IgG antibody 1:800 for IF (Jackson ImmunoResearch, 706-605-148), Alexa Fluor-647-conjugated donkey anti-rabbit IgG antibody 1:800 for IF (Jackson ImmunoResearch, 711-605-152), Alexa Fluor-647-conjugated donkey anti-mouse IgG antibody 1:800 for IF (Jackson ImmunoResearch, 715-605-151), Alexa Fluor-647-conjugated donkey anti-rat IgG antibody 1:800 for IF (Jackson ImmunoResearch, 712-605-153), Alexa Fluor-647-conjugated donkey anti-goat IgG antibody 1:800 for IF (Jackson ImmunoResearch, 705-605-147), Cy3-conjugated donkey anti-rabbit IgG antibody 1:800 for IF (Jackson ImmunoResearch, 711-165-152), Cy3-conjugated donkey anti-mouse IgG antibody 1:800 for IF (Jackson ImmunoResearch, 715-165-151), Cy3-conjugated donkey anti-guinea pig IgG antibody 1:800 for IF (Jackson ImmunoResearch, 706-165-148), Cy3-conjugated donkey anti-rat IgG antibody 1:800 for IF (Jackson ImmunoResearch, 712-165-153), Alexa Fluor-488-conjugated donkey anti-mouse IgG antibody 1:800 for IF (Jackson ImmunoResearch, 715-545-150), Alexa Fluor-488-conjugated donkey anti-guinea pig IgG antibody 1:800 for IF (Jackson ImmunoResearch, 706-545-148), Alexa Fluor-488-conjugated donkey anti-rabbit IgG antibody 1:800 for IF (Jackson ImmunoResearch, 711-545-152), donkey anti-mouse IgG antibody (Jackson ImmunoResearch, 715-005-151), donkey anti-rat IgG antibody (Jackson ImmunoResearch, 712-005-153), donkey anti-rabbit IgG antibody (Jackson ImmunoResearch, 711-005-152), donkey anti-chicken IgG antibody (Jackson ImmunoResearch, 703-005-155) . CF583R-conjugated secondary antibodies were made by conjugating the unlabeled secondary antibodies with CF583R succinimidyl ester (Biotium, 96084) to achieve a labeling efficiency of ~2 dyes per antibody, as previously described(*58*).

Lentivirus production and transduction of hippocampal neurons

Plasmids and gene segments used in this study were purchased from Addgene, GeneCopoeia, and Twist Bioscience, and subsequently cloned into the lentiviral expression vector FUGW (Addgene, Plasmid #14883), through Gibson assembly reaction (New England Biolabs, E5510S) according to the manufacturer's instructions. Coding sequences for CAV1, FLOT1, SH3GL1 (synthesized by Twist Bioscience), APP695 (Addgene, Plasmid #114193), and Basp1 (GenoCopoeia, Plasmid # EX-Mm10271-

M98) were fused to a C-terminal GFP via a flexible polypeptide linker and cloned into the FUGW vector, generating GFP-tagged constructs for caveolin-1, flotillin-1, endophilin-A2, APPwt and Basp1. Two point mutations (K670N and M671L) were introduced into APPwt-GFP to generate the familial Alzheimer's disease mutant APPswe-GFP construct. The coding sequence of Grm5a (Addgene, Plasmid #197305) was cloned into FUGW vector, with an HA tag inserted between Ser22 and Ser23 codons of Grm5a, as previously described(*43*), to generate HA-mGluR5a construct. The coding sequence of APP695 was cloned into FUGW vector, with SEP and BBS tags inserted as previously described(*59*), to generate SEP-APP construct.

Lentiviruses were produced by co-transfecting Lenti-X 293T cells with 6 μg lentiviral expression vector encoding the gene of interest, 4.5 μg Δ8.9 vector(*60*) (gift from Prof. David Baltimore, California Institute of Technology), and 3 μg VSVG packaging vector (Addgene, Plasmid #8454) in a 10 cm petri dish using Lipofectamine™ 3000 Transfection Reagent (Thermo Fisher Scientific, L3000008). One day before transfection, Lenti-X 293T cells were seeded in DMEM to reach ~80% confluency. One hour before transfection, the medium was replaced with viral packaging medium, which is Opti-MEM supplemented with 5% FBS and 200 μM sodium pyruvate. The first batch of viral supernatant was collected 24 hours post-transfection and stored at 4 °C, followed by replacement with fresh packaging medium was added to the cells. A second batch of supernatant was harvested 48 hours post-transfection, combined with the first batch, centrifuged at 1,500 g for 10 min, filtered through a 0.45 μm pore-size membrane (VWR, Inc.,76479-020), and concentrated using the Lenti-X concentrator (Clontech, 631231) at 4 °C overnight. The viral titers were determined before the samples were snap-frozen in liquid nitrogen. Lentiviruses were added to neuronal cultures at DIV 4-5.

Knockdown of βII-spectrin or CHC by shRNA adenovirus

The adenovirus expressing shRNA were purchased from SignaGen Laboratories. The sense sequences of the βII-spectrin shRNA are 5′-GCATGTCACGATGTTACAA-3′ and 5′-GGATGAAATGAAGGTGCTA-3′, as previously described(*61*). The sense sequence of CHC shRNA is 5'-GTTGGTGACCGTTGTTATG-3', as previously described(*42*). The adenovirus expressing a scramble shRNA sequence was used as a control (Vector BioLabs, 1122). Adenoviruses were added to the neuronal cultures at DIV 2 for βII-spectrin knockdown and at DIV 7 for CHC knockdown. The knockdown efficiencies were confirmed by immunofluorescence staining.

Neuron fixation and immunostaining for fluorescence imaging

Cultured hippocampal neurons were fixed using 4% (w/v) paraformaldehyde (PFA) in phosphate buffered saline (PBS) containing 4% (w/v) sucrose for 20 min at room temperature (RT). Following fixation,

neurons were washed three times in PBS, and permeabilized with 0.2 % (v/v) Triton X-100 in PBS for 10 min, unless otherwise stated. Neurons were then blocked in the blocking buffer containing 3% (wt/vol) bovine serum albumin (BSA) in PBS for 1 hour at RT, followed by incubation with primary antibodies diluted in blocking buffer overnight at 4°C. The following day, neurons were washed three times with PBS and incubated with fluorophore-conjugated secondary antibodies in blocking buffer for 1 hour at RT. After final washes in PBS, samples were processed for imaging.

For immunostaining of endogenous caveolin, neurons were first fixed with 4% (w/v) PFA at RT, followed by treatment with cold methanol at −20°C for 10 minutes. Neurons were then permeabilized with 0.2% (w/v) saponin in PBS for 10 minutes(*33*), followed by BSA blocking and incubation with primary and secondary antibodies using the protocol described above. For immunostaining of intracellular Aβ42, neurons were fixed with 4% (w/v) PFA and permeabilized with 0.2% (w/v) saponin in PBS for 10 minutes(*51*), followed by BSA blocking and incubation with primary and secondary antibodies using the protocol described above.

For dual-color staining of βII-spectrin and plasma membrane markers, wheat germ agglutinin (WGA) or cholera toxin subunit B (CTB), neurons were fixed with 4% (w/v) PFA in PBS, followed by incubation with 5 μg/mL AF647-conjugated WGA (Thermo Fisher Scientific, W32466) or 1 μg/mL AF647-conjugated CTB (Thermo Fisher Scientific, C34778) for 10 min. Neurons were then post-fixed with 4% PFA in PBS for 30 min, permeabilized with 0.2% (w/v) Triton X-100 in PBS for 10 min, and subsequently blocked and immunostained for βII-spectrin using primary and secondary antibodies.

For immunostaining of surface-expressed proteins including transferrin receptor (TfR), low-density lipoprotein receptor (LDLR), HA-mGluR5a, neural cell adhesion molecule 1 (NCAM1), and SEP-APP, neurons were fixed with 4% PFA in PBS without permeabilization, followed by BSA blocking and incubation with respective primary and secondary antibodies using the protocol described above. For immunostaining of phosphorylated ERK, neurons were fixed at various time points following ligand-induced ERK activation. Neurons were fixed with 4% PFA, followed by treatment with cold methanol at −20°C for 10 min and permeabilization with 0.2% Triton X-100 for 10 min before BSA blocking and incubation with primary and secondary antibodies, according to the manufacturer's instructions.

Western blotting of neuronal lysates

Neuronal cultures under each specified condition were lysed in RIPA buffer (Thermo Fisher Scientific, 89900), supplemented with 1x protease inhibitor cocktail (Thermo Fisher Scientific, 87786) and 1x phosphatase inhibitor cocktail (Thermo Fisher Scientific, 78420), following the manufacturer's instructions. The neuronal lysates were then centrifuged at 14,000g for 15 min at 4 °C to remove

insoluble debris, snap-frozen, and stored at −80 °C until use. Protein concentrations of neuronal culture lysates were determined by BCA protein assay kits (Thermo Fisher Scientific, 23227) with albumin standards, following the manufacturer's instructions. Equal protein amounts (20 μg per lane) were prepared in Laemmli buffer (Bio-Rad, 1610747) and resolved by SDS-PAGE on 4–20% gradient gels using a Tris–glycine running buffer (25 mM Tris, 192 mM Glycine, 0.1% SDS). Proteins were then transferred to PVDF membranes (Bio-Rad, 1620260) using the Trans-Blot Turbo transfer system (25 V, 1 A, 30 min). Membranes were processed with the Fast Western Kit (Thermo Fisher Scientific, 35060) and probed with mouse anti-αII-spectrin (EnCor Biotechnology, MCA-3D7) or mouse anti-βII-spectrin (BD Biosciences, 612563). Molecular weights of intact proteins and their breakdown products (BDPs) were assessed by comparison with molecular weight markers (Bio-Rad, 1610374).

Ligand-induced endocytosis assays

Transferrin and LDL endocytosis

Neuronal culture media were replaced with pre-warmed neurobasal medium (Thermo Fisher Scientific, 21103049) without supplements. Right after medium change, neurons were treated with 50 µg/mL CF568-conjugated transferrin (Biotium, 00083) or 10 µg/mL Dil-conjugated LDL (Thermo Fisher Scientific, L3482). At the indicated time points, neurons were quickly washed twice with ice-cold PBS, followed by three washes with ice-cold acid solution (150 mM glycine-HCl, pH 2.2)(*62*) to remove surface-bound fluorescent ligands, and three additional washes with ice-cold PBS. Neurons were then fixed with 4% (w/v) PFA in PBS containing 4% (w/v) sucrose for 20 min at RT. For transferrin uptake analysis, neurons were permeabilized with 0.2% (v/v) Triton X-100 for 10 min and immunostained with MAP2. For LDL uptake analysis, neurons were stained with AF647-conjugated CTB (Thermo Fisher Scientific, C34778) without the permeabilization step.

HA-mGluR5a endocytosis

Neuronal culture media were replaced with pre-warmed neurobasal medium without. Right after medium change, neurons expressing HA-mGluR5a through lentiviral transduction were treated with 5 µg/mL mouse anti-HA antibody. At the indicated time points, neurons were quickly washed twice with ice-cold PBS, followed by three washes with ice-cold acid solution and then three additional washes with ice-cold PBS. Neurons were then fixed with 4% PFA at RT for 20 min and incubated overnight at RT with 0.15 mg/mL unconjugated anti-mouse secondary antibody to block residual surface-bound anti-HA antibodies. After an additional 4% PFA fixation at RT for 30 min, neurons were permeabilized with 0.2% (v/v) saponin for 10 min, 3% (wt/vol) BSA in PBS for 1 hour at RT, and incubated with MAP2 primary antibody overnight at 4°C, followed by the incubation of secondary antibodies at RT for 60min for MAP2

and HA. For co-staining of endogenous caveolin, neurons were treated with cold methanol at -20 °C for 10 minutes prior to saponin permeabilization.

NCAM1 endocytosis

Neuronal culture media were replaced with pre-warmed neurobasal medium without supplements. Right after medium change, neurons were treated with 5 µg/mL rat anti-NCAM1 antibody. At the indicated time points, neurons were quickly washed three times with ice-cold PBS and fixed with 4% PFA for 20 min. To block surface-bound primary antibodies, neurons were incubated overnight at RT with 0.15 mg/mL Cy3-conjugated donkey anti-rat secondary antibody. After an additional 4% PFA fixation for 30 min, neurons were permeabilized with 0.2% Triton X-100 for 10 min, blocked with 3% (wt/vol) BSA in PBS for 1 hour at RT, and incubated with AF647-conjugated donkey anti-rat secondary antibody at RT for 60 min to detect internalized NCAM1(*63*). For co-staining of endogenous endophilin-A2 (EndoA2), neurons were incubated overnight at RT with 0.15 mg/mL unconjugated donkey anti-rat secondary antibody to block surface-bound primary antibodies, and neurons were additionally incubated with primary antibody against EndoA2 after Triton X-100 permeabilization, followed by secondary antibody incubation.

SEP-APP endocytosis

Neuronal culture media were replaced with pre-warmed neurobasal medium without supplements. Right after medium change, neurons expressing SEP-APP were treated with 0.5 µg/mL GFP nanobody (ProteinTech, gb2AF647-50). At the indicated time points, neurons were quickly washed twice with ice-cold PBS, followed by three washes with ice-cold acid solution, and three additional washes with ice-cold PBS. Neurons were then fixed with 4% PFA at RT and stained with AF647-CTB.

Pharmacological inhibition of endocytosis and protease activity

Neuronal culture media were replaced with pre-warmed neurobasal medium without supplements. To investigate the endocytic pathways involved in ligand-induced internalization, neurons were pretreated with 15 µM dyngo-4a (Cayman Chemical, 29479), 20 µM nystatin (Dot Scientific, DSN82020-5) or 40 µM EIPA (Cayman Chemical, 14406) for 30 min prior to ligand addition to investigate the endocytic pathways involved in ligand-induced internalization. To inhibit MEK activity, neurons were pretreated with 20 µM U0126 (Cell signaling, 9903S) for 15 min before ligand addition. To inhibit protease activity, neurons were treated with 50 µM MDL-28170 (Santa Cruz, sc-201301) or 50 µM Z-VAD-FMK (APExBIO, A1902-1) for 15 min before ligand addition to inhibit the calpain and caspase activities, respectively.

Widefield epi-fluorescence imaging

Widefield epi-fluorescence imaging was performed using a home-built microscope based on an Olympus IX-73 body, equipped with a 20x (N.A. 0.80) UPlanXApo air immersion objective, a 60x (N.A. 1.4) PlanApo oil immersion objective (Olympus), and a CMOS Camera (Thorlabs, CS126MU). A Lumencor SOLA light engine (SOLA U-nIR) was used as the light source for illumination. The 20x objective was used for imaging βII-spectrin, CHC, and surface receptors to quantify their expression levels. The average fluorescence intensity was quantified from 20-25 randomly selected imaging fields, with background fluorescence subtracted and the average fluorescence intensity normalized. The 60x objective was used for imaging LDL internalization, and the average area fraction of cellular area occupied by LDL endosomes was quantified from 20-25 randomly selected fields.

Confocal and structured illumination microscopy (SIM) imaging

Confocal and SIM imaging were performed using a custom microscope built on an Olympus IX-83 body, equipped with the CrestOptics X-Light V3 spinning disk confocal unit in combination with DeepSIM X-light super-resolution system module. Imaging was performed using either a 60× (N.A. 1.42) UPlanXApo or a 100× (N.A. 1.40) UPlanSApo oil immersion objective (Olympus), and an ORCA-Fusion BT digital CMOS camera (Hamamatsu, C15440-20UP). LDI-NIR-7 Laser Diode Illuminator (89 North) was used as the light source for illumination. For confocal imaging, images were acquired using Multi-Dimensional Acquisition module in Micro-Manager, with multi-color-channel acquisition and z-stack collection. AF488 (or GFP), Cy3 and AF647 were sequentially excited. Z-series images were collected from the top to the bottom of neurons, with a step size of 0.2-0.5 μm between planes. Final confocal images were reconstructed using maximum intensity z-projection. For SIM imaging, image acquisition and reconstruction were performed with the CrestOptics Super Resolution plugin integrated in Micro-Manager, allowing multi-color-channel SIM imaging. Stitching of SIM images was performed using the 'Grid/Collection stitching' plugin in ImageJ.

STORM imaging

The STORM setup was built on a Nikon Eclipse-Ti2 inverted microscope, equipped with a 100× (N.A. 1.45) Plan Apo oil-immersion objective (Olympus) and an EM-CCD camera (Andor iXon Life 897). 405-nm (Coherent, OBIS 405 nm LX, 1265577; 140 mW), 488-nm (Coherent, Sapphire 488-500 LPX CDRH, 1416094; 300 mW), 560-nm (MPB Communications Inc., 2RU-VFL-P-1500-560-B1R; 1500 mW) and 642-nm (MPB Communications Inc., 2RU-VFL-P-2000-642-B1R; 2000 mW) lasers were introduced through the back port of the microscope. The laser beams were shifted toward the edge of the objective to achieve near-total internal reflection (TIR) illumination, ensuring selective excitation of fluorophores within a few micrometers of the coverslip surface. For single-color 3D STORM imaging, AF647 was imaged. For dual-color STORM imaging, AF647 and CF583R were sequentially imaged as previously

described(*58*). A cylindrical lens was inserted into the detection path to introduce ellipticity into the point spread function, allowing determination of the z-positions of single molecules from the ellipticity of their images(*32*). Samples were imaged in an oxygen scavenging imaging buffer, containing 100 mM Tris-HCl (pH 7.5), 100 mM cysteamine (Sigma-Aldrich, G8270-100G), 5% (w/v) glucose (Sigma, G8270-100G), 0.8 mg/mL glucose oxidase (Sigma-Aldrich, G2133-10KU), and 40 µg/mL catalase (Sigma-Aldrich, C100-50MG). During imaging, continuous illumination of 642-nm or 560-nm laser (~2 kW/cm^2) was used to excite AF647 or CF583R molecules, respectively, switching them into the dark state. Continuous illumination of the 405-nm laser (0-1 W/cm^2) was used to reactivate the fluorophores to the emitting state, and the illumination power was controlled so that at any given time, only a small, optically resolvable fraction of the fluorophores in the field of view were in the emitting state. A typical single-color 3D STORM image was reconstructed from ~30,000 image frames acquired at a frame rate of 110 Hz. For dual-color 3D STORM, ~60,000 frames (30,000 per color-channel) were acquired under the same conditions. The recorded STORM movies were analyzed using established methods(*32*). Super-resolution images were reconstructed from the molecular coordinates by depicting each location as a 2D Gaussian peak. Color scale bar represents the z-coordinate information. For dual-color STORM analysis, each color-channel was processed independently, and the resulting images were aligned using fluorescent microspheres (Thermo Fisher Scientific, F8803) visible in both channels.

Data quantification and analysis

All subsequent data quantification and analyses were performed using custom MATLAB scripts.

Quantification of membrane-localized and internalized endocytic pits

50-100 randomly selected axon segments (~3 µm in length) and dendrite segments (~2 µm in length) were analyzed to determine the densities, lateral (*x/y* plane) and radical (*y/z* plane) distributions of endocytic pits in axonal and dendritic compartments, respectively. Single-molecule localizations of the MPS and endocytic pits from three-dimensional (3D) STORM images were analyzed using density-based spatial clustering of applications with noise (DBSCAN) algorithm to identify molecular clusters (i.e., endocytic pits) in 3D space. The volume of each endocytic pit was calculated using convex hull estimation. Following molecular cluster identification and removal of non-cluster noise, the single-molecule localizations of both MPS and endocytic pits were projected onto the *y/z* plane. Plasma membrane boundaries were delineated by generating *y/z* projections of the MPS localizations, followed by binary segmentation and elliptical fitting to define the plasma membrane contour. To quantitatively assess the subcellular localization of endocytic pits in the *y/z* cross-sectional view of neurites, we classified each endocytic pit as either surface-localized or internalized based on its spatial position relative to the neurite contour. Specifically, we defined two geometric parameters: d_1, the distance from

the centroid of an endocytic pit to the center of the fitted ellipse representing the neurite shape in the *y/z* view, and d_2, the distance from the fitted ellipse center to its boundary along the line connecting the ellipse center to the pit centroid. The ratio $d_1/d_2$was then used to determine localization. Endocytic pits with $d_1/d_2 < 0.75$ were classified as internalized, while those with $0.75 \leq d_1/d_2 \leq 1$ were considered surface-localized. Pits falling outside the neurite contour ($d_1/d_2 > 1$) were excluded from further analysis.

Analysis of spatial segregation between surface-localized endocytic pits and the MPS

Following clustering, single-molecule localizations of both MPS and surface-localized endocytic pits (single-molecule localizations for the internalized endocytic pits were removed) from dual-color 3D STORM images were projected onto the *x/y* plane and subsequently binarized. We used two complementary methods to validate the exclusion pattern between membrane-localized endocytic pits and the MPS. The first method is to quantify and compare Pearson's correlation coefficients (PCCs) between endocytic pits and the MPS under both experimental and randomized conditions. To assess statistical significance, spatial randomization was performed by repositioning each endocytic pit cluster within the boundary defined by the MPS regions, while avoiding overlaps between clusters. This randomization process was repeated 100 times to generate a null distribution of PCC values for the comparison with experimental data.

The alternative method is to generate averaged dual-color STORM images centered on individual endocytic pits. For each endocytic pit, the corresponding image—containing both the pit and its surrounding MPS structure—was aligned such that the centroid of the endocytic pit was placed at the center of a new composite frame. These frames were then merged into a composite image with intensity normalization for visualization. The final composite image was used to generate the radial intensity profiles of both MPS and endocytic pits, using the Radial Profile plugin in ImageJ.

Membrane-associated endocytic pits were classified into two categories based on their spatial relationship to the periodic MPS lattice: Class I pits that do not overlap with the MPS; and Class II pits that overlap with the MPS.

1D autocorrelation analysis

For One-dimensional (1D) autocorrelation analysis of the periodic MPS lattice in axons and dendrites, single-molecule localizations from STORM images were projected onto the longitudinal axis of randomly selected axon or dendrite segments. 1D autocorrelation functions were calculated from these 1D projected signals. To obtain the average autocorrelation function, the autocorrelation curves from 30-50 randomly selected axon segments (~2 μm in length) or dendrite segments (~3 μm in length) were averaged for

each condition. The average 1D autocorrelation amplitude was defined as the difference between the first peak (at ~190 nm) and the average of the two first valleys (at ~95 nm and ~285 nm) in the average 1D autocorrelation curve, which provides a quantitative measure of periodicity of the MPS lattice in neurites, as previously described(*15*).

Quantification of endocytic pit area fraction

The endocytic pit area fraction was defined as the ratio of the area occupied by endocytic pits to the area labeled by neuronal compartment markers, including neurofascin, tau, MAP2, CTB or surface NCAM1. For markers, images were first smoothed and binarized, after which the largest connected boundary was extracted and converted into a binary mask. This mask was then refined using hole filling and morphological closing to ensure accurate delineation of the neuronal compartments. For the endocytic pits, fluorescence signals within these marker-defined regions were processed by adaptive thresholding, followed by morphological opening to enhance puncta detection. Connected components were then filtered based on size criteria, and holes were filled to exclude incomplete detections. The average area fraction was calculated from 20–25 randomly selected imaging regions for each experimental condition.

Statistics

All experiments were independently replicated three times with similar results. In boxplots, the horizontal line represents the median, and the box denotes the interquartile range (IQR), with boundaries indicating the first and third quartiles. Whiskers extend to 1.5 × IQR, with potential outliers omitted. Data in the bar plots and time-course curves are presented as mean ± s.e.m. A two-sided, unpaired Student's *t*-test was used to assess statistical significance between two experimental conditions, and the corresponding *p*-values are indicated in the figures. A two-sided, paired Student's *t*-test was used to assess statistical significance between Pearson´s correlation coefficients under experimental and randomized conditions, and the corresponding *p*-values are indicated in the figures.

References

1. J. J. Rennick, A. P. R. Johnston, R. G. Parton, Key principles and methods for studying the endocytosis of biological and nanoparticle therapeutics. Nature Nanotechnology. 16, 266-276 (2021).
2. S. Camblor-Perujo, N. L. Kononenko, Brain-specific functions of the endocytic machinery. The FEBS Journal. 289, 2219-2246 (2022).
3. Ł. Zadka, M. Sochocka, N. Hachiya, J. Chojdak-Łukasiewicz, P. Dzięgiel, E. Piasecki, J. Leszek, Endocytosis and Alzheimer's disease. GeroScience. 46, 71-85 (2024).
4. S. Jaye, U. S. Sandau, J. A. Saugstad, Clathrin mediated endocytosis in Alzheimer's disease: cell type specific involvement in amyloid beta pathology. Front Aging Neurosci. 16, 1378576 (2024).
5. P. Hivare, K. Mujmer, G. Swarup, S. Gupta, D. Bhatia, Endocytic pathways of pathogenic protein aggregates in neurodegenerative diseases. Traffic. 24, 434-452 (2023).

6. C. Pathak, F. U. Vaidya, B. N. Waghela, P. K. Jaiswara, V. K. Gupta, A. Kumar, B. K. Rajendran, K. Ranjan, Insights of Endocytosis Signaling in Health and Disease. Int J Mol Sci. 24, (2023).
7. J. J. Thottacherry, M. Sathe, C. Prabhakara, S. Mayor, Spoiled for Choice: Diverse Endocytic Pathways Function at the Cell Surface. Annu Rev Cell Dev Biol. 35, 55-84 (2019).
8. H. T. McMahon, E. Boucrot, Molecular mechanism and physiological functions of clathrin-mediated endocytosis. Nature Reviews Molecular Cell Biology. 12, 517-533 (2011).
9. Z.-J. Cheng, R. Deep Singh, D. L. Marks, R. E. Pagano, Membrane microdomains, caveolae, and caveolar endocytosis of sphingolipids (Review). Molecular Membrane Biology. 23, 101-110 (2006).
10. L.-D. Popov, Deciphering the relationship between caveolae-mediated intracellular transport and signalling events. Cellular Signalling. 97, 110399 (2022).
11. S. Bodin, H. Elhabashy, E. Macdonald, D. Winter, C. Gauthier-Rouvière, Flotillins in membrane trafficking and physiopathology. Biology of the Cell. 117, e2400134 (2025).
12. E. Boucrot, A. P. A. Ferreira, L. Almeida-Souza, S. Debard, Y. Vallis, G. Howard, L. Bertot, N. Sauvonnet, H. T. McMahon, Endophilin marks and controls a clathrin-independent endocytic pathway. Nature. 517, 460-465 (2015).
13. G. Genet, K. Boyé, T. Mathivet, R. Ola, F. Zhang, A. Dubrac, J. Li, N. Genet, L. Henrique Geraldo, L. Benedetti, S. Künzel, L. Pibouin-Fragner, J.-L. Thomas, A. Eichmann, Endophilin-A2 dependent VEGFR2 endocytosis promotes sprouting angiogenesis. Nature Communications. 10, 2350 (2019).
14. K. Xu, G. Zhong, X. Zhuang, Actin, spectrin, and associated proteins form a periodic cytoskeletal structure in axons. Science. 339, 452-456 (2013).
15. G. Zhong, J. He, R. Zhou, D. Lorenzo, H. P. Babcock, V. Bennett, X. Zhuang, Developmental mechanism of the periodic membrane skeleton in axons. Elife. 3, e04581 (2014).
16. C. Leterrier, J. Potier, G. Caillol, C. Debarnot, F. Rueda Boroni, B. Dargent, Nanoscale Architecture of the Axon Initial Segment Reveals an Organized and Robust Scaffold. Cell Rep. 13, 2781-2793 (2015).
17. E. D'Este, D. Kamin, F. Gottfert, A. El-Hady, S. W. Hell, STED nanoscopy reveals the ubiquity of subcortical cytoskeleton periodicity in living neurons. Cell Rep. 10, 1246-1251 (2015).
18. B. Han, R. Zhou, C. Xia, X. Zhuang, Structural organization of the actin-spectrin-based membrane skeleton in dendrites and soma of neurons. Proc Natl Acad Sci U S A. 114, E6678-E6685 (2017).
19. E. D'Este, D. Kamin, C. Velte, F. Gottfert, M. Simons, S. W. Hell, Subcortical cytoskeleton periodicity throughout the nervous system. Sci Rep. 6, 22741 (2016).
20. J. He, R. Zhou, Z. Wu, M. A. Carrasco, P. T. Kurshan, J. E. Farley, D. J. Simon, G. Wang, B. Han, J. Hao, E. Heller, M. R. Freeman, K. Shen, T. Maniatis, M. Tessier-Lavigne, X. Zhuang, Prevalent presence of periodic actin-spectrin-based membrane skeleton in a broad range of neuronal cell types and animal species. Proc Natl Acad Sci U S A. 113, 6029-6034 (2016).
21. E. D'Este, D. Kamin, F. Balzarotti, S. W. Hell, Ultrastructural anatomy of nodes of Ranvier in the peripheral nervous system as revealed by STED microscopy. Proc Natl Acad Sci U S A. 114, E191-E199 (2017).
22. M. Hauser, R. Yan, W. Li, N. A. Repina, D. V. Schaffer, K. Xu, The Spectrin-Actin-Based Periodic Cytoskeleton as a Conserved Nanoscale Scaffold and Ruler of the Neural Stem Cell Lineage. Cell Rep. 24, 1512-1522 (2018).
23. R. Zhou, B. Han, C. Xia, X. Zhuang, Membrane-associated periodic skeleton is a signaling platform for RTK transactivation in neurons. Science. 365, 929-934 (2019).
24. D. Albrecht, C. M. Winterflood, M. Sadeghi, T. Tschager, F. Noe, H. Ewers, Nanoscopic compartmentalization of membrane protein motion at the axon initial segment. J Cell Biol. 215, 37-46 (2016).
25. M. Hammarlund, E. M. Jorgensen, M. J. Bastiani, Axons break in animals lacking beta-spectrin. J Cell Biol. 176, 269-275 (2007).
26. M. Krieg, A. R. Dunn, M. B. Goodman, Mechanical control of the sense of touch by beta-spectrin. Nat Cell Biol. 16, 224-233 (2014).

27. R. Zhou, B. Han, R. Nowak, Y. Lu, E. Heller, C. Xia, A. H. Chishti, V. M. Fowler, X. Zhuang, Proteomic and functional analyses of the periodic membrane skeleton in neurons. Nature Communications. 13, 3196 (2022).
28. N. Unsain, M. D. Bordenave, G. F. Martinez, S. Jalil, C. von Bilderling, F. M. Barabas, L. A. Masullo, A. D. Johnstone, P. A. Barker, M. Bisbal, F. D. Stefani, A. O. Caceres, Remodeling of the Actin/Spectrin Membrane-associated Periodic Skeleton, Growth Cone Collapse and F-Actin Decrease during Axonal Degeneration. Sci Rep. 8, 3007 (2018).
29. G. Wang, D. J. Simon, Z. Wu, D. M. Belsky, E. Heller, M. K. O'Rourke, N. T. Hertz, H. Molina, G. Zhong, M. Tessier-Lavigne, X. Zhuang, Structural plasticity of actin-spectrin membrane skeleton and functional role of actin and spectrin in axon degeneration. Elife. 8, e38730 (2019).
30. F. Wernert, S. B. Moparthi, F. Pelletier, J. Lainé, E. Simons, G. Moulay, F. Rueda, N. Jullien, S. Benkhelifa-Ziyyat, M.-J. Papandréou, C. Leterrier, S. Vassilopoulos, The actin-spectrin submembrane scaffold restricts endocytosis along proximal axons. Science. 385, eado2032 (2024).
31. M. J. Rust, M. Bates, X. Zhuang, Sub-diffraction-limit imaging by stochastic optical reconstruction microscopy (STORM). Nature Methods. 3, 793-796 (2006).
32. B. Huang, W. Wang, M. Bates, X. Zhuang, Three-Dimensional Super-Resolution Imaging by Stochastic Optical Reconstruction Microscopy. Science. 319, 810-813 (2008).
33. O. O. Glebov, N. A. Bright, B. J. Nichols, Flotillin-1 defines a clathrin-independent endocytic pathway in mammalian cells. Nature Cell Biology. 8, 46-54 (2006).
34. S. Sabharanjak, P. Sharma, R. G. Parton, S. Mayor, GPI-Anchored Proteins Are Delivered to Recycling Endosomes via a Distinct cdc42-Regulated, Clathrin-Independent Pinocytic Pathway. Developmental Cell. 2, 411-423 (2002).
35. M. Shikanai, Y. V. Nishimura, M. Sakurai, Y. I. Nabeshima, M. Yuzaki, T. Kawauchi, Caveolin-1 Promotes Early Neuronal Maturation via Caveolae-Independent Trafficking of N-Cadherin and L1. iScience. 7, 53-67 (2018).
36. Y. M. Sigal, R. Zhou, X. Zhuang, Visualizing and discovering cellular structures with super-resolution microscopy. Science. 361, 880-887 (2018).
37. X. Chen, S. Zhong, Y. Hou, R. Cao, W. Wang, D. Li, Q. Dai, D. Kim, P. Xi, Superresolution structured illumination microscopy reconstruction algorithms: a review. Light: Science & Applications. 12, 172 (2023).
38. S. Liu, P. Hoess, J. Ries, Super-Resolution Microscopy for Structural Cell Biology. Annual Review of Biophysics. 51, 301-326 (2022).
39. A. McCluskey, J. A. Daniel, G. Hadzic, N. Chau, E. L. Clayton, A. Mariana, A. Whiting, N. N. Gorgani, J. Lloyd, A. Quan, L. Moshkanbaryans, S. Krishnan, S. Perera, M. Chircop, L. von Kleist, A. B. McGeachie, M. T. Howes, R. G. Parton, M. Campbell, J. A. Sakoff, X. Wang, J.-Y. Sun, M. J. Robertson, F. M. Deane, T. H. Nguyen, F. A. Meunier, M. A. Cousin, P. J. Robinson, Building a Better Dynasore: The Dyngo Compounds Potently Inhibit Dynamin and Endocytosis. Traffic. 14, 1272-1289 (2013).
40. P. L. Cameron, T. C. Südhof, R. Jahn, P. De Camilli, Colocalization of synaptophysin with transferrin receptors: implications for synaptic vesicle biogenesis. Journal of Cell Biology. 115, 151-164 (1991).
41. M. D. Brown, G. A. Banker, I. M. Hussaini, S. L. Gonias, S. R. VandenBerg, Low density lipoprotein receptor-related protein is expressed early and becomes restricted to a somatodendritic domain during neuronal differentiation in culture. Brain Research. 747, 313-317 (1997).
42. S. Watanabe, T. Trimbuch, M. Camacho-Pérez, B. R. Rost, B. Brokowski, B. Söhl-Kielczynski, A. Felies, M. W. Davis, C. Rosenmund, E. M. Jorgensen, Clathrin regenerates synaptic vesicles from endosomes. Nature. 515, 228-233 (2014).
43. L. Fourgeaud, A.-S. Bessis, F. Rossignol, J.-P. Pin, J.-C. Olivo-Marin, A. Hémar, The Metabotropic Glutamate Receptor mGluR5 Is Endocytosed by a Clathrin-independent Pathway *. Journal of Biological Chemistry. 278, 12222-12230 (2003).

44. S. N. Rai, H. Dilnashin, H. Birla, S. S. Singh, W. Zahra, A. S. Rathore, B. K. Singh, S. P. Singh, The Role of PI3K/Akt and ERK in Neurodegenerative Disorders. Neurotoxicity Research. 35, 775-795 (2019).
45. F. H. Kobeissy, M. C. Liu, Z. Yang, Z. Zhang, W. Zheng, O. Glushakova, S. Mondello, J. Anagli, R. L. Hayes, K. K. W. Wang, Degradation of βII-Spectrin Protein by Calpain-2 and Caspase-3 Under Neurotoxic and Traumatic Brain Injury Conditions. Molecular Neurobiology. 52, 696-709 (2015).
46. S. Zadran, H. Jourdi, K. Rostamiani, Q. Qin, X. Bi, M. Baudry, Brain-derived neurotrophic factor and epidermal growth factor activate neuronal m-calpain via mitogen-activated protein kinase-dependent phosphorylation. J Neurosci. 30, 1086-1095 (2010).
47. S. Zhuang, Y. Yan, R. A. Daubert, J. Han, R. G. Schnellmann, ERK promotes hydrogen peroxide-induced apoptosis through caspase-3 activation and inhibition of Akt in renal epithelial cells. American Journal of Physiology-Renal Physiology. 292, F440-F447 (2007).
48. E. Nakajima, K. B. Hammond, T. R. Shearer, M. Azuma, Activation of the mitochondrial caspase pathway and subsequent calpain activation in monkey RPE cells cultured under zinc depletion. Eye. 28, 85-92 (2014).
49. T. Burrinha, C. Guimas Almeida, Aging impact on amyloid precursor protein neuronal trafficking. Current Opinion in Neurobiology. 73, 102524 (2022).
50. J. Aow, T.-R. Huang, Y. T. Goh, A. X. Sun, G. Thinakaran, E. H. Koo, Evidence for a clathrin-independent endocytic pathway for APP internalization in the neuronal somatodendritic compartment. Cell Reports. 42, 112774 (2023).
51. T. Burrinha, I. Martinsson, R. Gomes, A. P. Terrasso, G. K. Gouras, C. G. Almeida, Upregulation of APP endocytosis by neuronal aging drives amyloid-dependent synapse loss. Journal of Cell Science. 134, (2021).
52. P. Kienlen-Campard, S. Miolet, B. Tasiaux, J.-N. Octave, Intracellular Amyloid-β1–42, but Not Extracellular Soluble Amyloid-β Peptides, Induces Neuronal Apoptosis*. Journal of Biological Chemistry. 277, 15666-15670 (2002).
53. F. M. LaFerla, K. N. Green, S. Oddo, Intracellular amyloid-β in Alzheimer's disease. Nature Reviews Neuroscience. 8, 499-509 (2007).
54. W. A. Eimer, R. Vassar, Neuron loss in the 5XFAD mouse model of Alzheimer's disease correlates with intraneuronal Aβ42 accumulation and Caspase-3 activation. Mol Neurodegener. 8, 2 (2013).
55. J. S. Morrow, M. C. Stankewich, The Spread of Spectrin in Ataxia and Neurodegenerative Disease. Journal of experimental neurology. 2, 131 - 139 (2021).
56. J. H. Su, M. Zhao, A. J. Anderson, A. Srinivasan, C. W. Cotman, Activated caspase-3 expression in Alzheimer’s and aged control brain: correlation with Alzheimer pathology. Brain Research. 898, 350-357 (2001).
57. X. X. Yan, A. Jeromin, A. Jeromin, Spectrin Breakdown Products (SBDPs) as Potential Biomarkers for Neurodegenerative Diseases. Curr Transl Geriatr Exp Gerontol Rep. 1, 85-93 (2012).
58. B. Wang, M. Xiong, J. Susanto, X. Li, W.-Y. Leung, K. Xu, Transforming Rhodamine Dyes for (d)STORM Super-Resolution Microscopy via 1,3-Disubstituted Imidazolium Substitution. Angewandte Chemie International Edition. 61, e202113612 (2022).
59. J. Aow, T.-R. Huang, G. Thinakaran, E. H. Koo, Enhanced cleavage of APP by co-expressed Bace1 alters the distribution of APP and its fragments in neuronal and non-neuronal cells. Molecular Neurobiology. 59, 3073-3090 (2022).
60. C. Lois, E. J. Hong, S. Pease, E. J. Brown, D. Baltimore, Germline Transmission and Tissue-Specific Expression of Transgenes Delivered by Lentiviral Vectors. Science. 295, 868-872 (2002).
61. Mauricio R. Galiano, S. Jha, Tammy S.-Y. Ho, C. Zhang, Y. Ogawa, K.-J. Chang, Michael C. Stankewich, Peter J. Mohler, Matthew N. Rasband, A Distal Axonal Cytoskeleton Forms an Intra-Axonal Boundary that Controls Axon Initial Segment Assembly. Cell. 149, 1125-1139 (2012).
62. N. Kamei, S. Yamamoto, H. Hashimoto, M. Nishii, M. Miyaura, K. Tomada, I. Nakase, M. Takeda-Morishita, Optimization of the method for analyzing endocytosis of fluorescently tagged molecules:

Impact of incubation in the cell culture medium and cell surface wash with glycine-hydrochloric acid buffer. Journal of Controlled Release. 310, 127-140 (2019).
63. N. L. Carrodus, K. S.-L. Teng, K. M. Munro, M. J. Kennedy, J. M. Gunnersen, Differential Labeling of Cell-surface and Internalized Proteins after Antibody Feeding of Live Cultured Neurons. JoVE. e51139 (2014).
64. H. Babcock, jeffmoffitt, A. Boettiger, G. Emanuel, leonardosepulveda, gtdempsey, T. Kayikcioglu. (Zenodo, 2019).
65. J. Fei, R. Zhou. (Zenodo, 2025).

Acknowledgments

Funding

This work was supported by NIH R35 GM142973 (R.Z.), the Life Sciences Research Foundation (R.Z.), and the startup fund from the Pennsylvania State University (R.Z.).

Author contributions

Conceptualization: J.F., and R.Z. Methodology: J.F., and R.Z. Investigation: J.F., Y.Z., C.L., and R.Z. Data curation: J.F., Y.Z, and R.Z. Validation: J.F., Y.Z., C.L., and R.Z. Visualization: J.F., and R.Z. Formal analysis: J.F., Y.Z., C.L., and R.Z. Funding acquisition: R.Z. Resources: J.F., and R.Z. Supervision: J.F., and R.Z. Project administration: J.F., and R.Z. Writing—original draft: J.F., and R.Z. Writing—review and editing: J.F., Y.Z., Y.T., and R.Z. Software: J.F., and Y.T.

Competing interests

The authors declare no competing interests.

Data and code availability

All data needed to evaluate and reproduce the results in the paper are present in the paper or the Supplementary Materials. Custom Python and MATLAB codes for image acquisition and STORM analysis are available at https://github.com/ZhuangLab (DOI: 10.5281/zenodo.3264857)(*64*) and https://github.com/thezhoulab/ (DOI: 10.5281/zenodo.17656223(*65*).

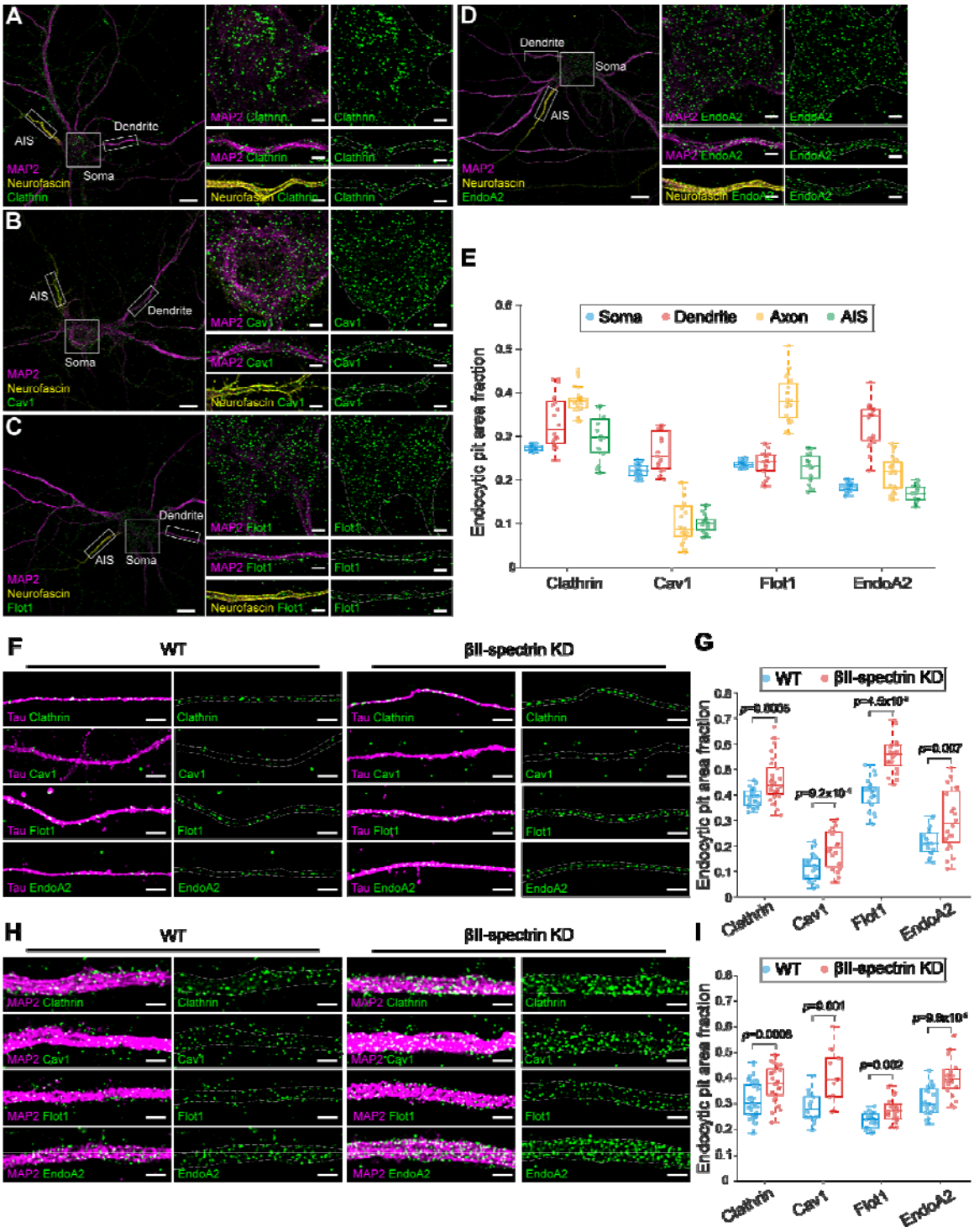

Fig. 1. Compartment-resolved mapping of four endocytic pit types reveals broad suppression of basal endocytosis by the MPS in neurons. (**A-D**) Left: Stitched SIM images showing the distributions of endogenous endocytic pits, clathrin (**A**), Cav1(**B**), Flot1 (**C**) or EndoA2 (**D**) in WT neurons. Endocytic

pits are shown in green, with compartment markers MAP2 (magenta) and neurofacsin (yellow). Scale bar: 10 µm. Right: Enlarged SIM images of the three boxed regions on the left, corresponding to soma, dendrite and AIS compartments, respectively. Scale bar: 2 µm. (**E**) Boxplots showing the area fraction of endogenous endocytic pits in different compartments of WT neurons. (**F**) Left: SIM images of tau (magenta) and endogenous endocytic pits (green) in distal axons of WT neurons. Right: Same as Left, but in βII-spectrin knockdown (KD) neurons. Scale bars: 2 µm. (**G**) Boxplots showing the area fraction of endogenous endocytic pits (green) in distal axons of WT and βII-spectrin KD neurons. (**H**) Left: SIM images of MAP2 (magenta) and endogenous endocytic pits (green) in dendrites of WT neurons. Right: Same as Left, but in βII-spectrin KD neurons. Scale bars: 2 µm. (**I**) Boxplots showing the area fraction of endogenous endocytic pits in dendrites of WT and βII-spectrin KD neurons.

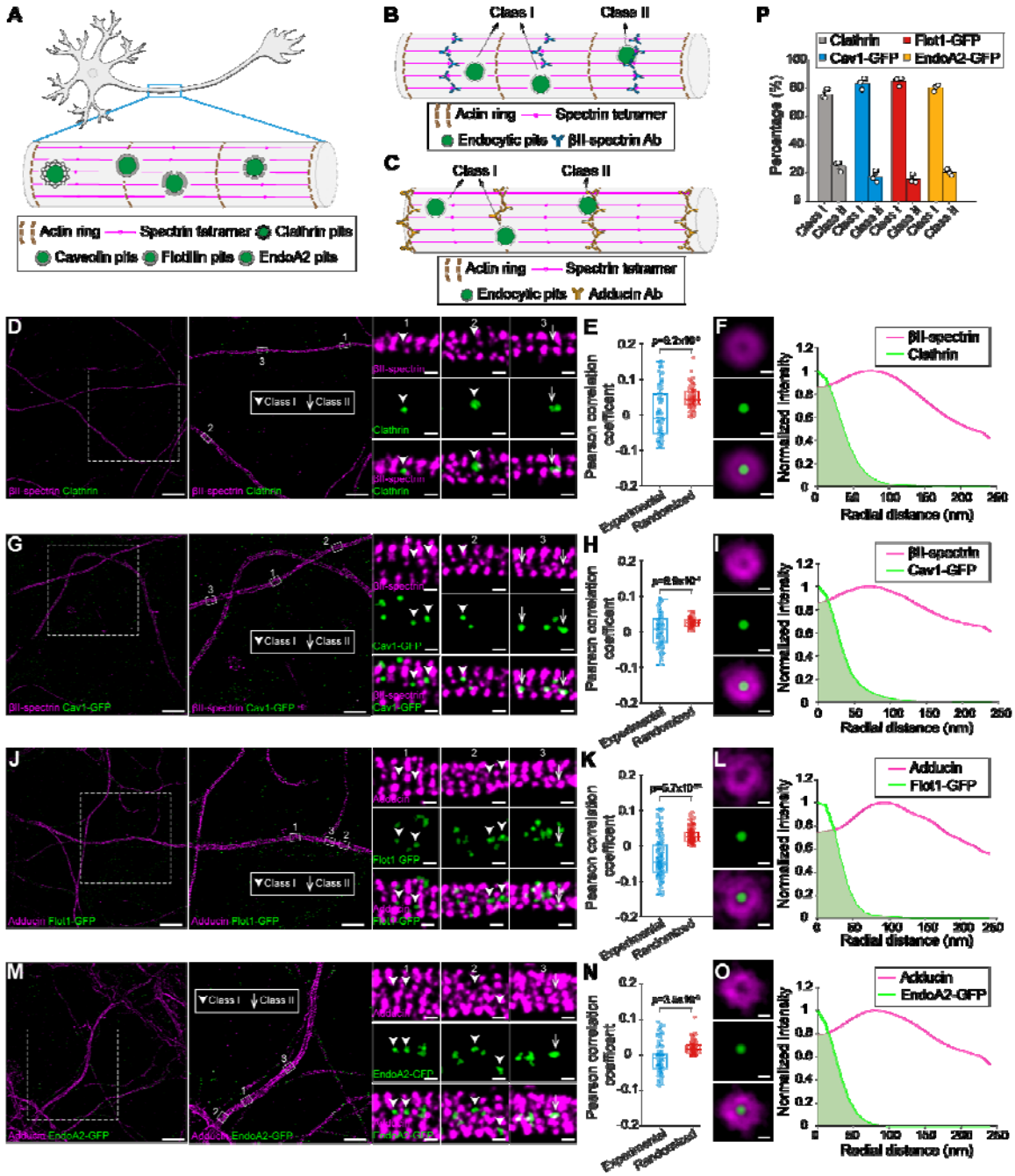

Fig. 2. Four major types of endocytic pits are localized within "clearings" of the MPS lattice in axons. (**A**) Schematic illustrating the spatial distributions of clathrin, Cav1, Flot1 and EndoA2 endocytic pits, relative to periodic MPS lattice in axons. (**B**) Schematic illustrating two distinct types of endocytic pits based on their spatial positioning relative to periodic βII-spectrin lattice in axons. Class I pits do not overlap with MPS lattice, whereas Class II do. The MPS was visualized by immunostaining with antibodies targeting the C-terminus of βII-spectrin, which mark the centers of spectrin tetramers. (**C**) Same as in (B) but showing spatial relationships with the periodic adducin lattice in axons. The MPS was

visualized by immunostaining with antibodies targeting the adducin, which mark the terminal ends of spectrin tetramers. (**D**) Left: Dual-color STORM images of βII-spectrin (magenta) and endogenous clathrin (green) in axons. Right: Magnified views of Class I and Class II clathrin-coated pits (CCPs) in the boxed regions. Scale bars: 10 µm (left), 5 µm (middle), 200 nm (right). (**E**) Pearson correlation coefficients between βII-spectrin and endogenous clathrin under experimental and randomized conditions. (**F**) Left: Averaged dual-color STORM images of βII-spectrin (magenta) and endogenous clathrin (green), generated by aligning individual STORM images to the centers of CCPs. Right: Radial intensity profiles of the averaged images shown on the left. Scale bar: 100 nm. (**G-I**) Same as in (**D–F**), but for βII-spectrin (magenta) and exogenously expressed Cav1 (green). (**J-L**) Same as in (**D–F)**, but for adducin (magenta) and exogenously expressed Flot1 (green). (**M-O**) Same as in (**D–F)**, but for adducin (magenta) and exogenously expressed EndoA2 (green). (**P**) Percentages of Class I and Class II pits for endogenous clathrin, exogenously expressed Cav1, exogenously expressed Flot1 and exogenously expressed EndoA2 in axons.

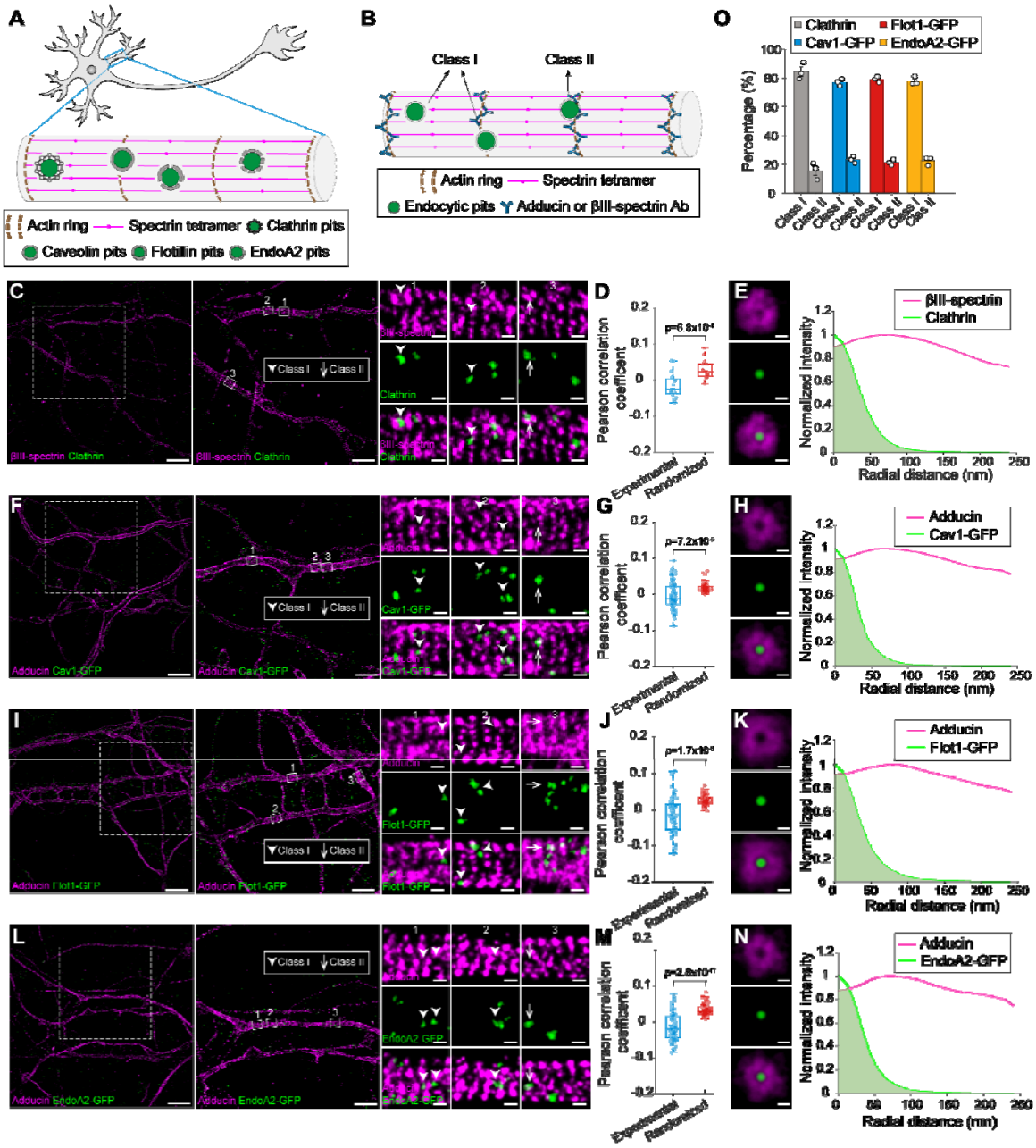

Fig. 3. Four major types of endocytic pits are localized within "clearings" of the MPS lattice in dendrites. (**A**) Schematic illustrating the spatial distribution of clathrin, Cav1, Flot1 and EndoA2 endocytic pits, relative to periodic MPS lattice in dendrites. (**B**) Schematic illustrating two distinct types of endocytic pits based on their spatial positioning relative to periodic βIII-spectrin or adducin lattice in dendrites. Class I pits do not overlap with MPS lattice, whereas Class II pits do. The MPS was visualized by immunostaining with antibodies targeting the N-terminus of βIII-spectrin or adducin, which both mark terminal ends of spectrin tetramers. (**C**) Left: Dual-color STORM images of βIII-spectrin (magenta) and endogenous clathrin (green) in dendrites. Right: Magnified views of Class I and Class II clathrin-coated pits (CCPs) in the boxed regions. Scale bars: 10 µm (left), 5 µm (middle), 200 nm (right). (**D**) Pearson correlation coefficients between βIII-spectrin and endogenous clathrin under experimental and randomized conditions. (**E**) Left: Averaged dual-color STROM images of βIII-spectrin (magenta) and endogenous clathrin (green), generated by aligning individual STORM images to the centers of CCPs.

Right: Radial intensity profile of averaged images shown on the left. Scale bar: 100 nm. **(F-H**) Same as in (**C–E)**, but for adducin (magenta) and exogenously expressed Cav1 (green). **(I-K)** Same as in (**C–E**), but for adducin (magenta) and exogenously expressed Flot1 (green). (**L-N**) Same as in (**C–E**), but for adducin (magenta) and exogenously expressed EndoA2 (green). (**O**) Percentages of Class I and Class II endocytic pits for endogenous clathrin, exogenously expressed Cav1, exogenously expressed Flot1 and exogenously expressed EndoA2 in dendrites.

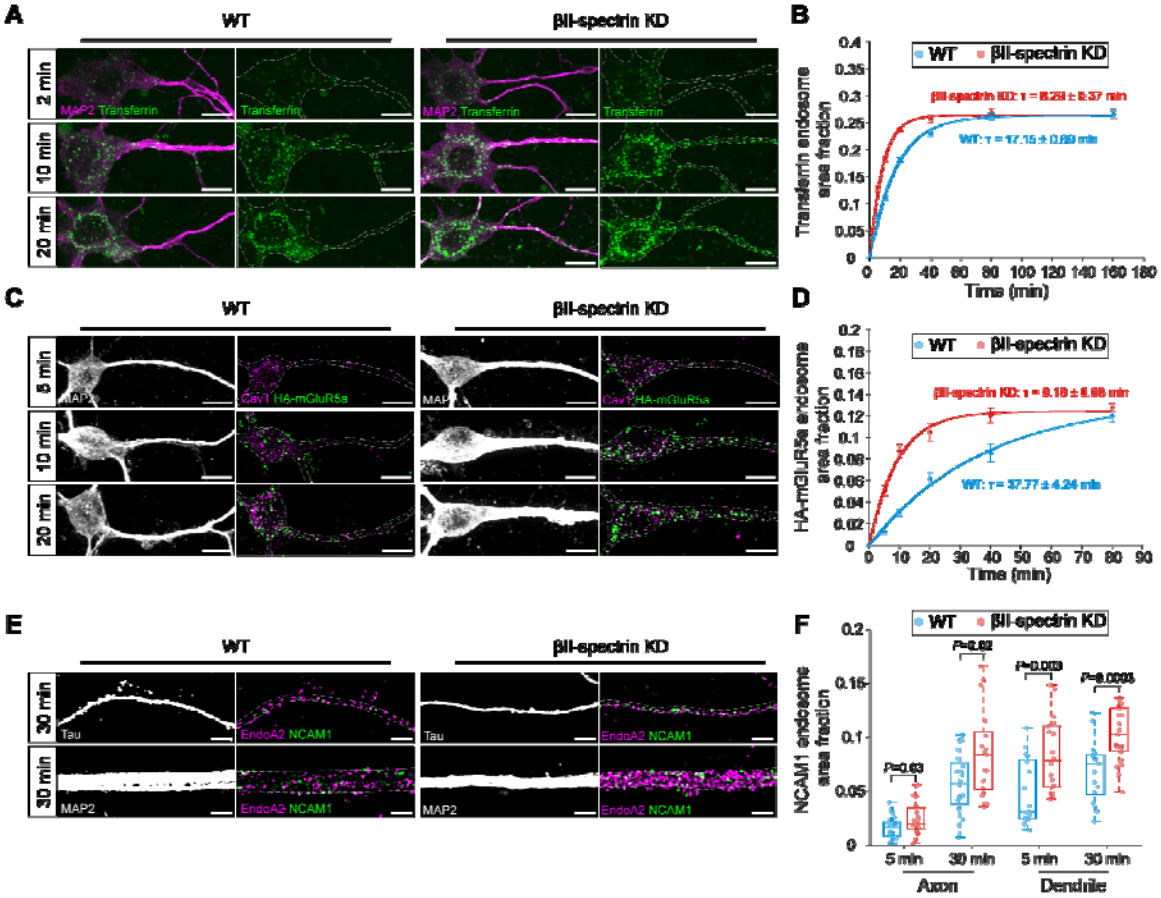

Fig. 4. MPS inhibits ligand-induced endocytosis in both axonal and somatodendritic compartments. (**A**) Confocal fluorescence images of MAP2 (magenta) and internalized CF568-transferrin (green) in somatodendritic region of WT or βII-spectrin KD neurons treated with CF568-transferrin for 2, 10, and 20 minutes. Scale bars: 10 µm. (**B**) Time course of CF568-transferrin endocytosis in somatodendritic regions of WT and βII-spectrin KD neurons, quantified by the area fraction of transferrin-positive endosomes. Solid lines represent single-exponential fits to the data. (**C**) Confocal fluorescence images of MAP2 (gray), internalized HA-mGluR5a (green) and endogenous Cav1 (magenta) in somatodendritic region of WT or βII-spectrin KD neurons overexpressing HA-mGluR5a and treated with anti-HA antibody for 5, 10, and 20 minutes. Scale bars: 10 µm. (**D**) Time course of Cav1-mediated HA-mGluR5a endocytosis in the somatodendritic regions of WT and βII-spectrin KD neurons, quantified by the area fraction of Cav1-positive HA-mGluR5a endosomes. Solid lines represent single-exponential fits to the data. (**E**) SIM images of internalized NCAM1 (green) and endogenous endoA2 (magenta) in axonal (top) and somatodendritic region (bottom) of WT or βII-spectrin KD neurons treated with anti-NCAM1 antibody for 30 minutes. Scale bars: 2 µm. (**F**) Boxplots of EndoA2-mediated NCAM1 endocytosis in axonal and somatodendritic regions of WT and βII-spectrin KD neurons, quantified by the area proportion of EndoA2-positive NCAM1 endosomes.

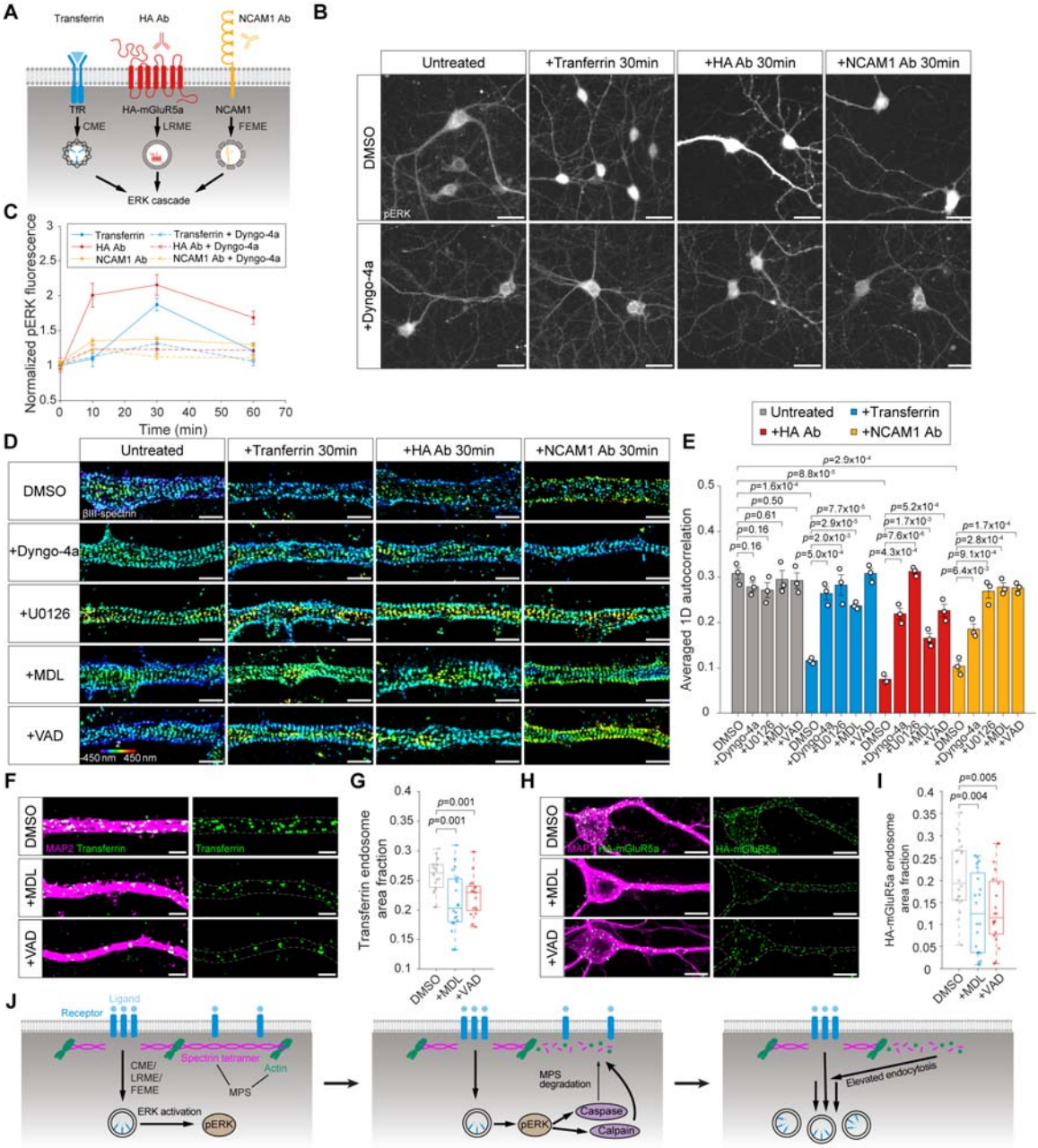

Fig. 5. The MPS acts as a dynamic barrier modulated by endocytosis and ERK signaling through a positive feedback mechanism. (**A**) Schematic illustrating ligand-induced ERK activation via three major endocytic pathways: CME of transferrin receptor, LRME of HA-mGluR5a, and FEME of NCAM1. (**B**) Top: Epi-fluorescence images showing pERK immunostaining in neurons without ligand treatment, neurons treated with CF568-transferrin, and neurons overexpressing HA-mGluR5a treated with anti-HA antibody. Bottom: Same as the top, but with neurons pretreated with dyngo-4a before ligand treatment. Scale bars: 25 µm. (**C**) Time course of ERK activation in neurons under the same conditions as in (**B**). (**D**) 3D STORM images of immunostained βIII-spectrin in dendrites of neurons under various treatments. First column: neurons pretreated with DMSO, dyngo-4a, U0126, MDL or VAD. Second column: neurons pretreated with the same inhibitors followed by CF568-transferrin treatment. Third column: neurons overexpressing HA-mGluR5a pretreated with the same inhibitors followed by the anti-HA antibody treatment. Fourth column: neurons pretreated with the same inhibitors followed by anti-NCAM1 antibody

treatment. Scale bars: 1 µm. Color scale bar represents the z-coordinate information. (**E**) Averaged 1D autocorrelation amplitudes of βIII-spectrin, calculated for the same conditions as in (**D**). (**F**) SIM images of MAP2 (magenta) and internalized CF568-transferrin (green) in neurons pretreated with DMSO, MDL or VAD followed by CF568-transferrin treatment. Scale bars: 2 µm. (**G**) Boxplots of transferrin-positive endosome area fractions. (**H**) Confocal fluorescence images of MAP2 (magenta) and internalized HA-mGluR5a (green) in neurons overexpressing HA-mGluR5a pretreated with DMSO, MDL or VAD followed by anti-HA antibody treatment. Scale bars: 10 µm. (**I**) Boxplots of HA-mGluR5a endosome area fractions. (**J**) Schematic summarizing the proposed positive feedback mechanism: receptor endocytosis via CME, LRME, or FEME activates ERK signaling, which triggers calpain- and caspase-mediated MPS degradation; MPS disruption in turn facilitates further endocytosis, establishing a positive feedback loop.

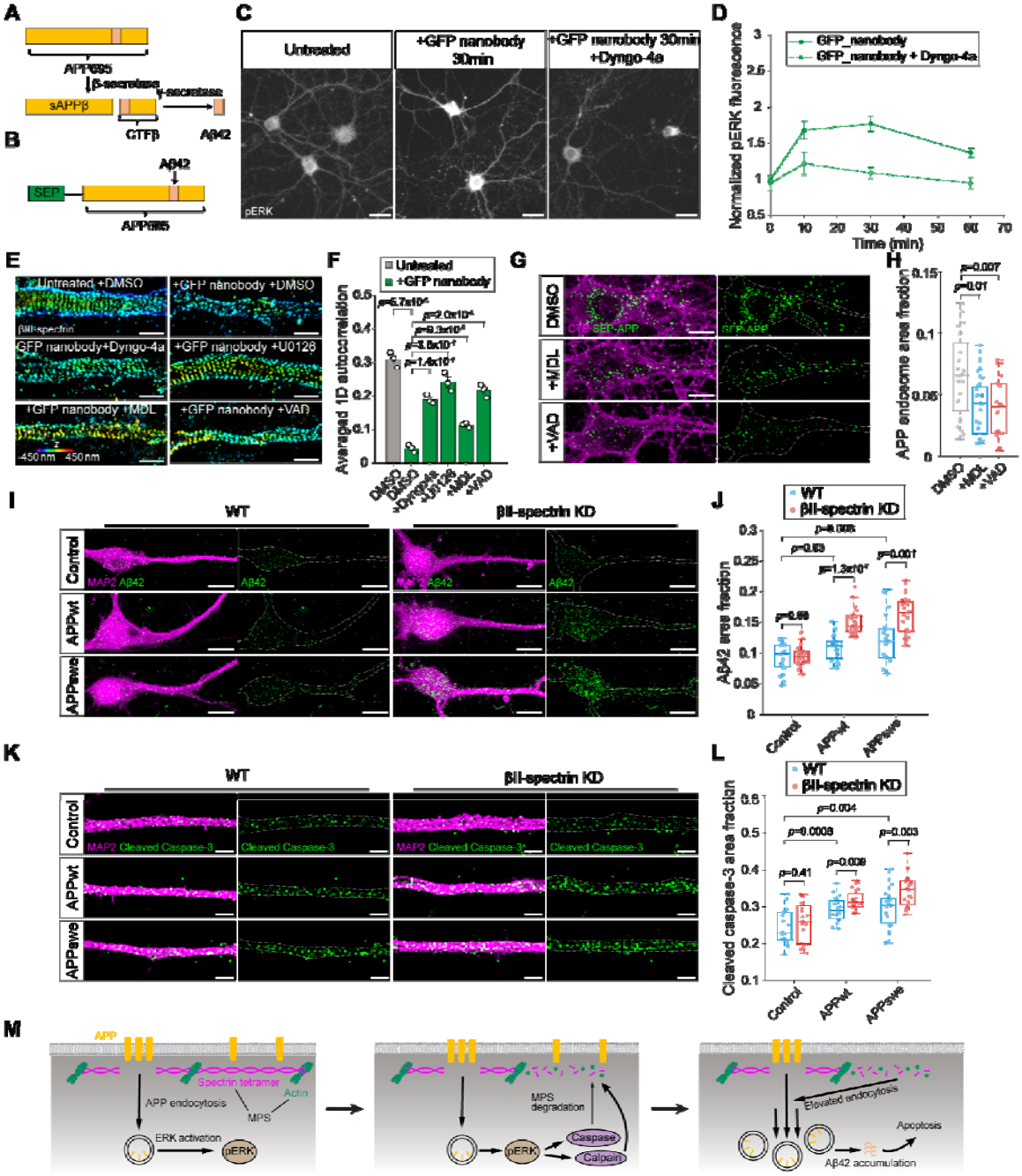

Fig. 6. The MPS serves as a neuroprotective barrier by restricting APP endocytosis and Aβ42 accumulation. (**A**) Schematic illustrating the sequential cleavage of APP695 by β-secretase and γ-secretase to produce Aβ42. (**B**) Schematic illustrating the structure of SEP-APP. (**C**) Left: Epi-fluorescence images of pERK in neurons overexpressing SEP-APP without ligand treatment. Middle: Same as left, but treated with GFP nanobody. Right: Same as middle, but with dyngo-4a pre-incubation before GFP nanobody treatment. Scale bars: 25 µm. (**D**) Time course of ERK activation in neurons under the same conditions as in (**C**). (**E**) 3D STORM images of immunostained βIII-spectrin in dendrites of neurons pretreated with DMSO, dyngo-4a, U0126, MDL or VAD followed by GFP nanobody treatment. Scale bars: 1 µm. (**F**) Averaged 1D autocorrelation amplitude of βIII-spectrin, calculated for the same conditions as in (**E**). (**G**) Confocal fluorescence images of CTB (magenta) and internalized SEP-APP (green) in neurons pretreated with DMSO, MDL or VAD followed by GFP nanobody treatment. Scale

bars: 10 µm. (**H**) Boxplots of SEP-APP endosome area fractions. (**I**) Left: Confocal fluorescence images of MAP2 (magenta) and intracellular Aβ42 (green) in WT neurons, neurons overexpressing APPwt, and neurons overexpressing APPswe. Right: Same as left, but in βII-spectrin KD neurons. Scale bars: 10 µm. (**J**) Boxplots of intracellular Aβ42 area fractions in somatodendritic regions of neurons. (**K**) Left: SIM images of MAP2 (magenta) and cleaved caspase-3 (green) in WT neurons, neurons overexpressing APPwt , and neurons overexpressing APPswe. Right: Same as left, but in βII-spectrin KD neurons. Scale bars: 2 µm. (**L**) Boxplots of cleaved caspase-3 area fractions in dendrites of neurons. (**M**) Schematic illustrating APP endocytosis triggers downstream ERK signaling, leading to MPS degradation through caspase- and calpain-mediated spectrin cleavage. This degradation further accelerates APP endocytosis, promoting intracellular Aβ42 accumulation and caspase-3 activation.

Supplementary Materials for

Membrane-associated periodic skeleton regulates major forms of endocytosis in neurons through a signaling-driven positive feedback loop

Jinyu Fei *et al.*

*Corresponding author. Email: ruobo.zhou@psu.edu

This PDF file includes:

Fig. S1 to S10

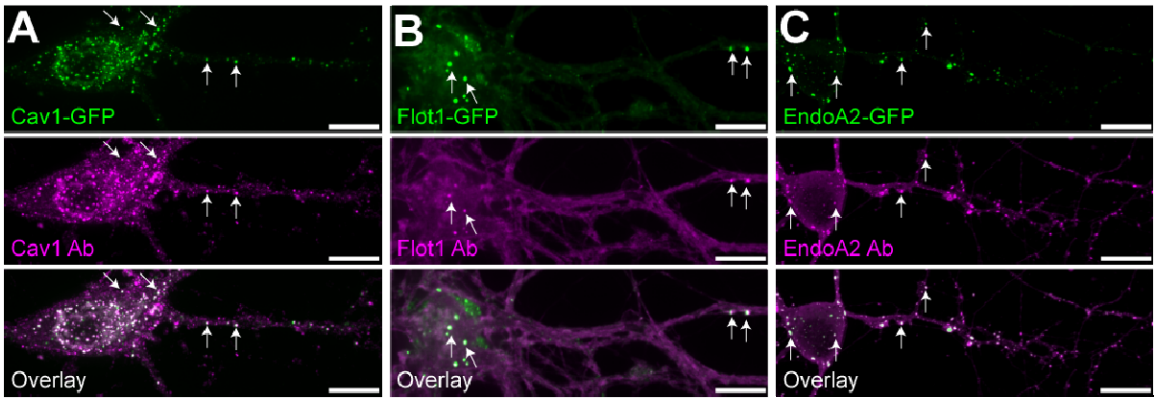

Fig. S1. Validation of antibodies and immunofluorescence-based labeling of caveolin-, flotillin-, and endophilinA2-positive endocytic pits, related to Fig. 1. (**A**) Confocal fluorescence images of neurons exogenously expressing GFP-tagged Cav1 and immunostained for Cav1. Regions of strong colocalization are indicated by white arrows. (**B**) Same as (**A**), but for neurons exogenously overexpressing GFP-tagged Flot1 and immunostained for Flot1. (**C**) Same as (**A**), but for neurons exogenously expressing GFP-tagged EndoA2 and immunostained for EndoA2. Scale bars: 10 µm.

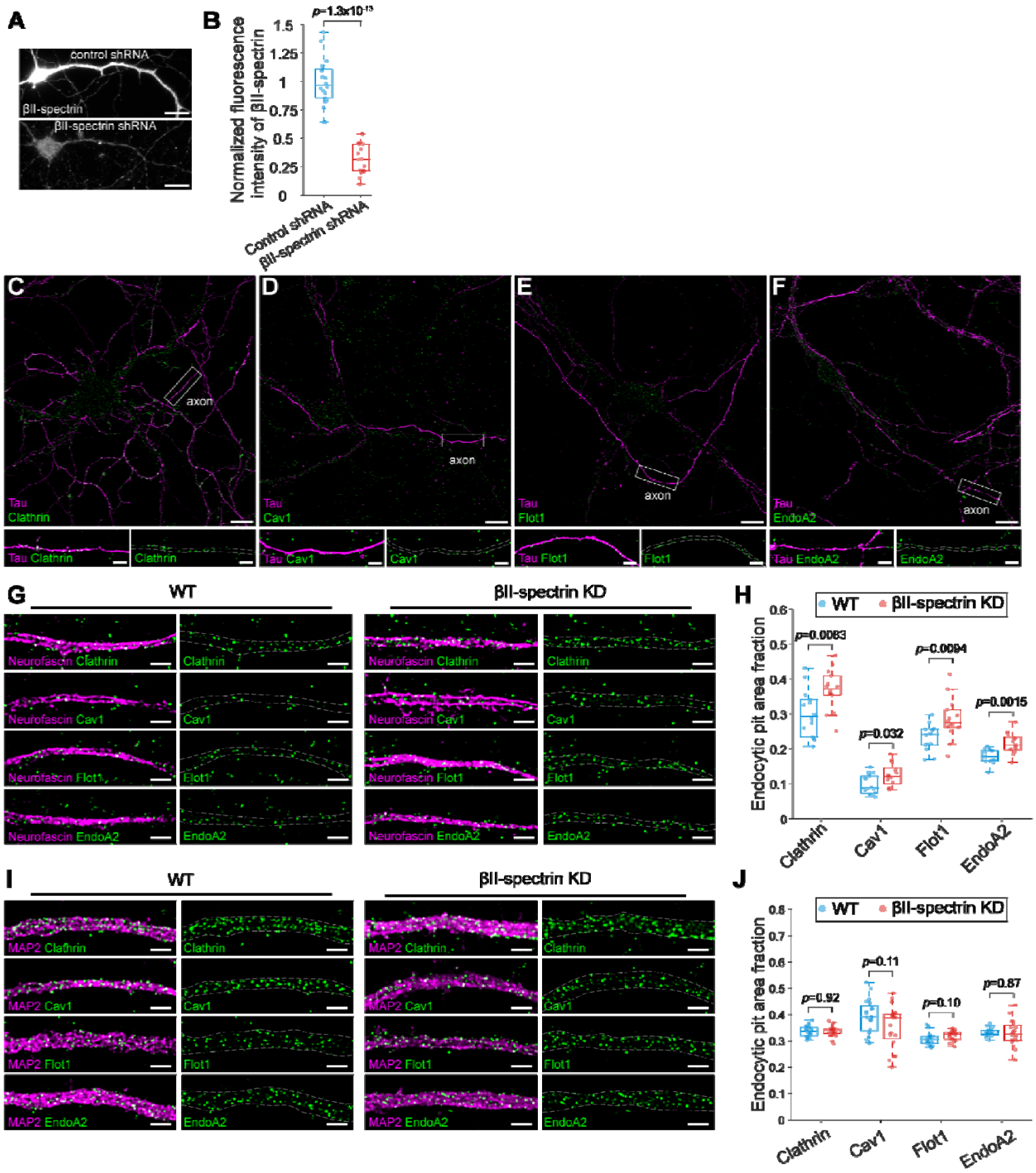

Fig. S2. Basal endocytosis activities in distal axons and the effect of MPS disruption on the basal endocytosis in the Axon Initial Segment (AIS), related to Fig. 1. (**A**) Widefield epi-fluorescence images of βII-spectrin in neurons transduced with adenoviruses expressing either scrambled (control) shRNA or βII-spectrin shRNA. Scale bar: 25 µm. (**B**) Boxplots showing the normalized fluorescence intensity of βII-spectrin. (**C-F**) Stitched SIM images showing the distributions of endogenous endocytic pits, clathrin (**C**), Cav1(**D**), Flot1 (**E**), or EndoA2 (**F**) in wild-type (WT) neurons. Endocytic pits are shown in green, tau, a distal axon marker, is shown in magenta. Scale bar: 10 µm. Bottom: Enlarged SIM

images of the boxed regions on the top, corresponding to distal axon compartments. Scale bar: 2 µm. (**G)** Left: SIM images of neurofascin (magenta) and endogenous endocytic pits (green; clathrin, Cav1, Flot1, or EndoA2) at the AIS of WT neurons. Right: Same as Left, but in βII-spectrin knockdown (KD) neurons. Scale bars: 2 µm. (**H**) Boxplots showing the area fraction of endogenous endocytic pits at the AIS of WT and βII-spectrin KD neurons. (**I)** Left: SIM images of MAP2 (magenta) and endogenous endocytic pits (green) in dendrites of WT neurons (DIV 7). Right: Same as Left, but in βII-spectrin knockdown (KD) neurons (DIV 7). Scale bars: 2 µm. (**J**) Boxplots showing the area fraction of endogenous endocytic pits in dendrites of WT and βII-spectrin KD neurons (DIV 7). Boxplots show the median and boundaries (first and third quartile); Whiskers denote 1.5 times the interquartile range of the box. *p*-values calculated with two-sided unpaired Student's *t*-test.

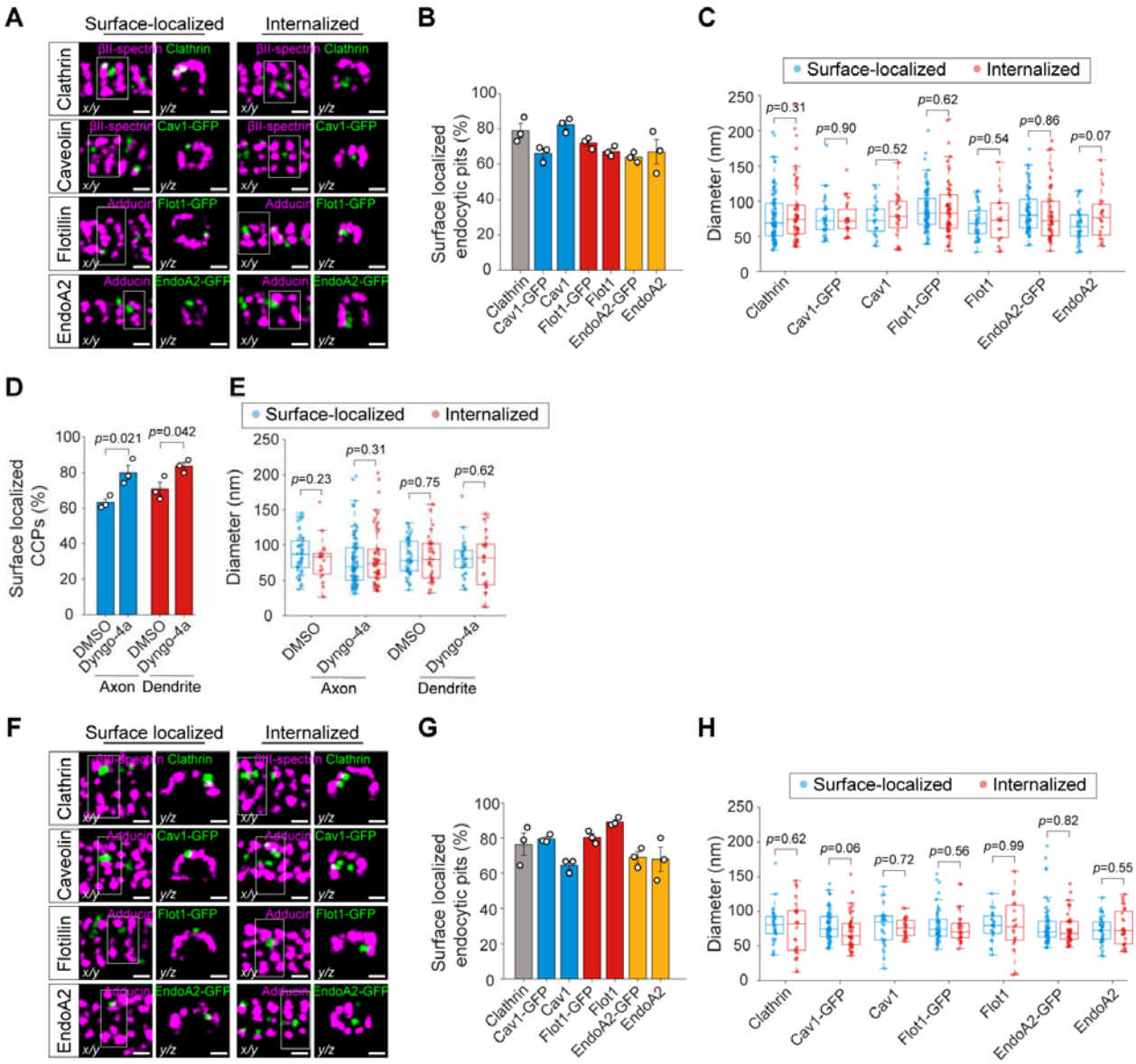

Fig. S3. Quantification of surface-localized and internalized endocytic pits in axons and dendrites, related to Fig. 2 and Fig. 3. (**A**) Left: Representative dual-color STORM images of the MPS (magenta) and surface-localized endocytic pits (green) in axons. Endogenous clathrin and exogenously expressed Cav1 were co-stained with βII-spectrin, while exogenously expressed Flot1 and exogenously expressed EndoA2 were co-stained with adducin. The *y/z* view corresponds to the white-boxed region in the *x/y* view. Right: Same as Left, but for endocytic pits internalized within the axonal cytoplasm. Scale bars: 200 nm. (**B**) Average percentage of surface-localized endocytic pits in axons. Quantification includes only endogenous clathrin, and both endogenous and exogenously expressed Cav1, Flot1, and EndoA2. (**C**) Boxplots showing the diameters of surface-localized and internalized endocytic pits in axons. Quantification includes the same categories as in (**B**). (**D**) Average percentage of surface-localized CCPs in axons and dendrites under DMSO (control) or dyngo-4a treatment. (**E**) Boxplots showing the diameters of membrane-localized and internalized CPPs in axons and dendrites under DMSO or dyngo-4a treatment. (**F-H**) Same as (**A-C**), but for dendrites. Data are presented as mean ± s.e.m. (n = 3 biological replicates

per condition). Boxplots show the median and boundaries (first and third quartile); Whiskers denote 1.5 times the interquartile range of the box. *p*-values calculated with two-sided unpaired Student's *t*-test.

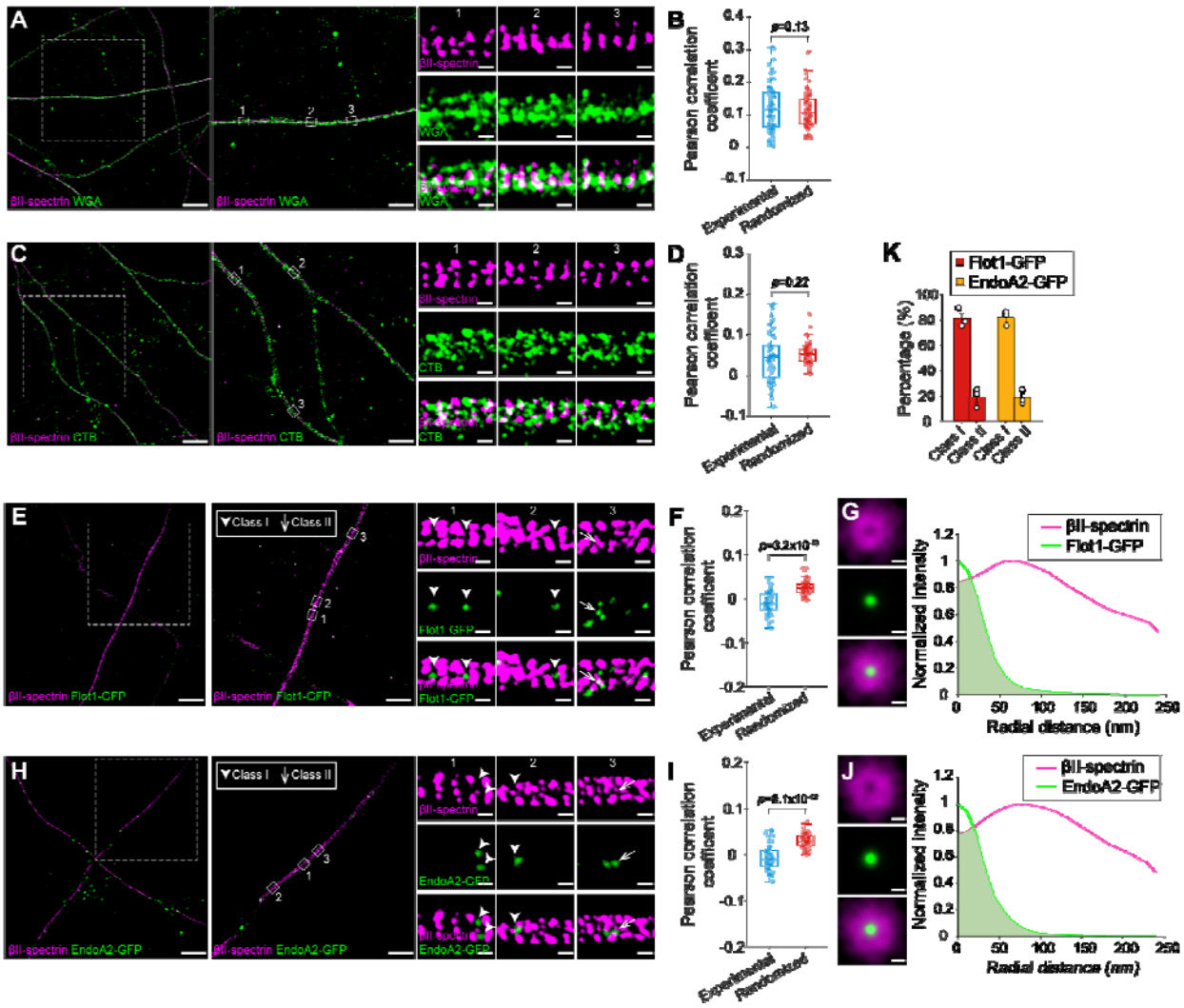

Fig. S4. Endocytic pits are localized within "clearings" of the MPS lattice in axons, related to Fig. 2. (**A**) Dual-color STORM images of βII-spectrin (magenta) and wheat germ agglutinin (WGA, green) in axons. Scale bars: 10 µm (left), 5 µm (middle), 200 nm (right). (**B**) Pearson correlation coefficients between βII-spectrin and WGA under experimental and randomized conditions. (**C, D**) Same as (**A, B**), but for βII-spectrin (magenta) and cholera toxin subunit B (CTB, green). (**E**) Left: Dual-color STORM images of βII-spectrin (magenta) and exogenously expressed Flot1 (green) in axons. Right: Magnified views of Class I and Class II Flot1-pits in the boxed regions. Scale bars: 10 µm (left), 5 µm (middle), 200 nm (right). (**F**) Pearson correlation coefficients between βII-spectrin and exogenously expressed Flot1 under experimental and randomized conditions. (**G**) Left: Averaged dual-color STORM images of βII-spectrin (magenta) and exogenously expressed Flot1 (green), generated by aligning individual STORM images to the centers of Flot1-pits. Right: Radial intensity profiles of the averaged images shown on the left. Scale bar: 100 nm. (**H-J**) Same as in (**E–G**), but for βII-spectrin (magenta) and exogenously expressed EndoA2 (green). (**K**) Percentages of Class I and Class II pits for exogenously expressed Flot1 and exogenously expressed EndoA2 in axons. Data are presented as mean ± s.e.m. (n = 3 biological replicates per condition). Boxplots show the median and boundaries (first and third quartile); Whiskers denote 1.5 times the interquartile range of the box. p-values calculated with two-sided paired Student's t-test.

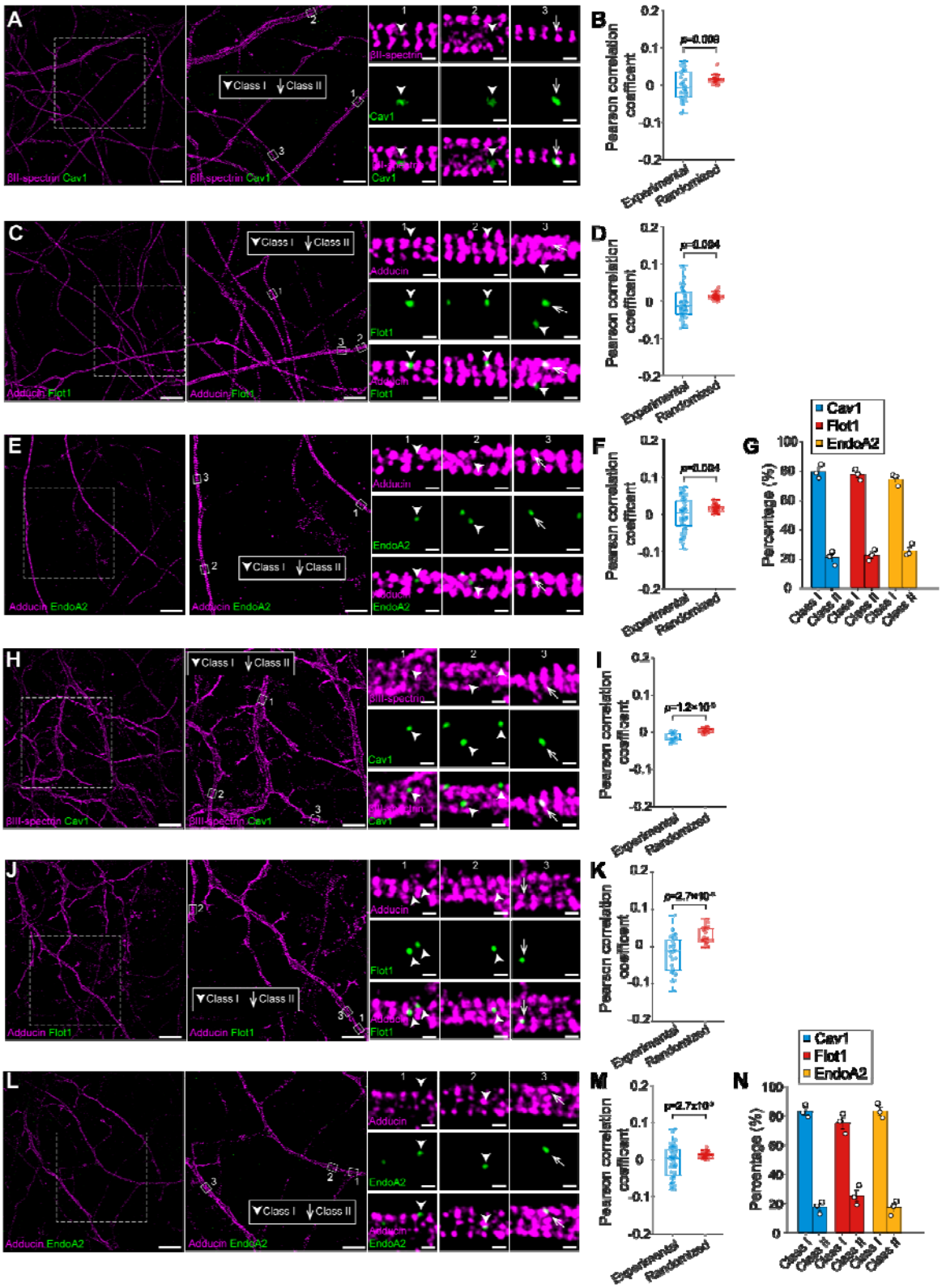
A
B
C
D
E
F
G
H
I
J
K
L
M
N
Class I
Class II
βII-spectrin
Cav1
Adducin
Flot1
EndoA2
Pearson correlation coefficient
Experimental
Randomized
Percentage (%)
Cav1
Flot1
EndoA2

Fig. S5. Endogenous endocytic pits are localized within "clearings" of the MPS lattice in axons and dendrites, related to Fig. 2 and Fig. 3. (**A**) Left: Dual-color STORM images of βII-spectrin (magenta) and endogenous Cav1 (green) in axons. Right: Magnified views of Class I and Class II Cav1-pits in the boxed regions. Scale bars: 10 µm (left), 5 µm (middle), 200 nm (right). (**B**) Pearson correlation coefficients between βII-spectrin and endogenous Cav1 under experimental and randomized conditions. (**C, D**) Same as (**A, B**), but for adducin (magenta) and endogenous Flot 1 (green). **(E, F**) Same as (**A, B**), but for adducin (magenta) and endogenous EndoA2 (green). (**G)** Percentages of Class I and Class II pits for endogenous Cav1, endogenous Flot1 and endogenous EndoA2 in axons. (**H**) Left: Dual-color STORM images of βIII-spectrin (magenta) and endogenous Cav1 (green) in dendrites. Right: Representative enlarged images of Class I and Class II Cav1-pits from the boxed regions. Scale bars: 10 µm (left), 5 µm (middle), 200 nm (right). (**I**) Pearson correlation coefficients between βIII-spectrin and endogenous Cav1 under experimental and randomized conditions. (**J, K**) Same as in (**H, I**), but for adducin (magenta) and endogenous Flot1 (green) in dendrites. (**L, M**) Same as in (**H, I**), but for adducin (magenta) and endogenous EndoA2 (green) in dendrites. (**N)** Percentages of Class I and Class II pits for endogenous Cav1, endogenous Flot1 and endogenous EndoA2 in dendrites. Data are presented as mean ± s.e.m. (n = 3 biological replicates per condition). Boxplots show the median and boundaries (first and third quartile); Whiskers denote 1.5 times the interquartile range of the box. p-values calculated with two-sided paired Student's t-test.

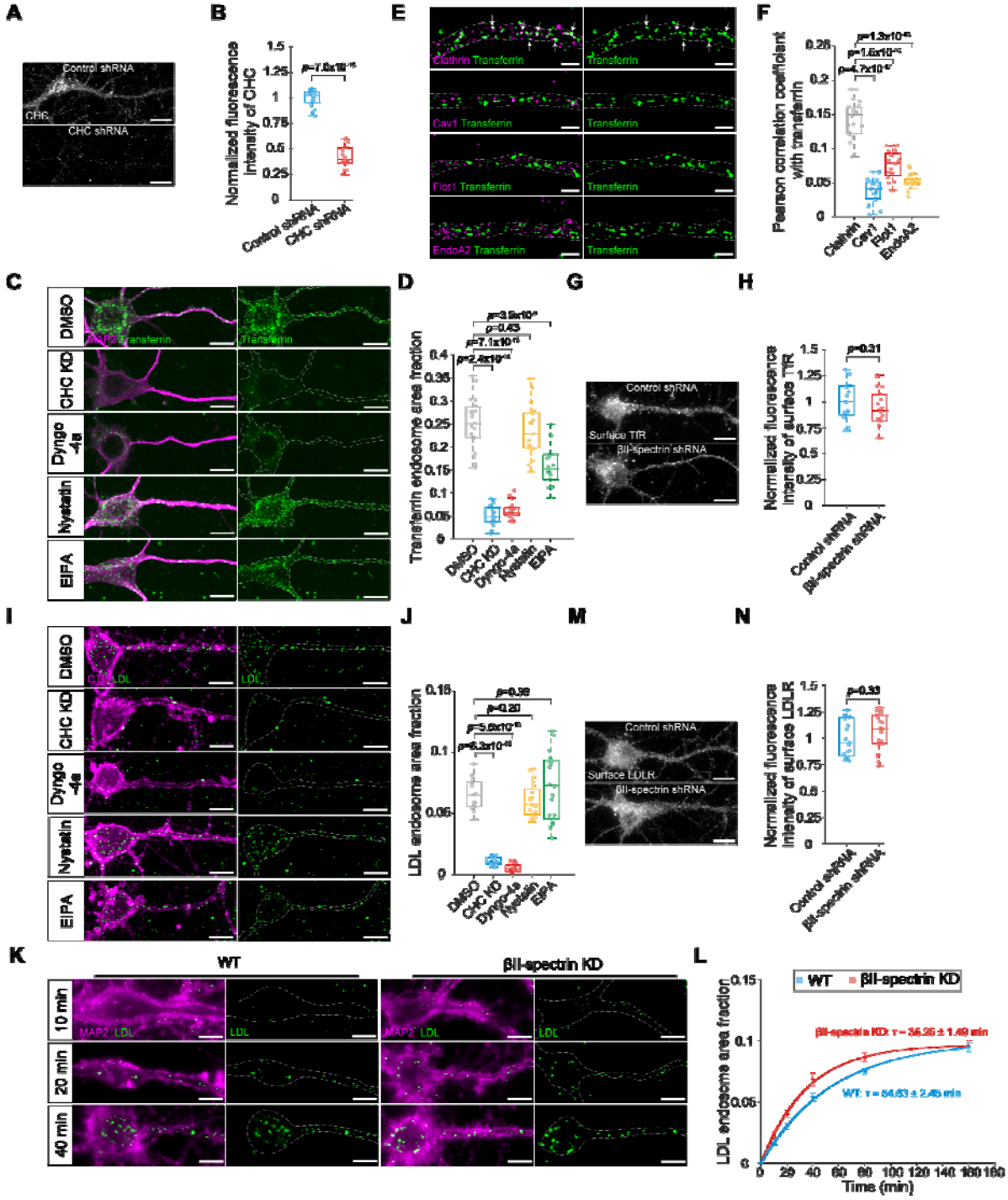

Fig. S6. Endocytic pathways for transferrin and LDL endocytosis and the effect of MPS disruption on LDL endocytosis, related to Fig. 4. (**A**) Widefield epi-fluorescence images of clathrin heavy chain (CHC) in neurons transduced with adenoviruses expressing either scrambled (control) shRNA or CHC shRNA. Scale bars: 25 µm. (**B**) Boxplots showing the normalized fluorescence intensity of CHC. (**C**) Confocal fluorescence images of MAP2 (magenta) and internalized CF568-transferrin (green) in somatodendritic region of CHC KD neurons pretreated with DMSO followed by CF568-transferrin treatment for 40 minutes, and WT neurons pretreated with DMSO, dyngo-4a, nystatin or EIPA for 30

minutes, followed by CF568-transferrin treatment for 40 minutes. Scale bars: 10 µm. (**D**) Boxplots of CF568-transferrin endocytosis in somatodendritic regions of neurons, quantified by the area fraction of transferrin endosomes. (**E**) Dual-color SIM images of internalized CF568-transferin (green) and endocytic pits (magenta; clathrin, Cav1, Flot1 or EndoA2) in dendrites of WT neurons treated with CF568-transferrin for 30 minutes. Regions of strong colocalization are indicated by white arrows. Scale bars: 2 µm. (**F**) Pearson correlation coefficients between internalized CF568-transferrin and endocytic pits. (**G**) Widefield epi-fluorescence images of surface-localized transferrin receptor (TfR) in WT and βII-spectrin KD neurons without ligand stimulation. Surface-localized TfR was immunostained with anti-TfR antibody following cell fixation without Triton permeabilization. Scale bars: 25 µm. (**H)** Boxplots showing the normalized fluorescence intensity of surface TfR. (**I**) Widefield epi-fluorescence images of CTB (magenta) and internalized Dil-LDL (green) in somatodendritic region of CHC KD neurons pretreated with DMSO, followed by treatment with Dil-LDL for 40 minutes, and WT neurons pretreated with DMSO, dyngo-4a, nystatin or EIPA for 30 minutes, followed by treatment with Dil-LDL for 40 minutes. Scale bars: 10 µm. (**J**) Boxplots of Dil-LDL endocytosis in somatodendritic regions of neurons, quantified by the area fraction of LDL endosomes. (**K**) Left: Widefield epi-fluorescence images of internalized Dil-LDL in somatodendritic regions of WT neurons treated with Dil-LDL for 10, 20 and 40 minutes. Right: Same as Left, but in βII-spectrin KD neurons. Scale bars: 10 µm. (**L**) Time course of LDL endocytosis in the somatodendritic regions of WT and βII-spectrin KD neurons, quantified by the area fraction of LDL endosomes. Solid lines represent single-exponential fits. Data are presented as mean ± s.e.m. (**M**) Widefield epi-fluorescence images of surface-localized LDLR in WT and βII-spectrin KD neurons without ligand stimulation. Surface-localized LDLR was immunostained with anti-LDLR antibody following cell fixation without Triton permeabilization. Scale bars: 25 µm. (**N**) Boxplots showing the normalized fluorescence intensity of surface LDLR. Boxplots show the median and boundaries (first and third quartile); Whiskers denote 1.5 times the interquartile range of the box. *p*-values calculated with two-sided unpaired Student's *t*-test.

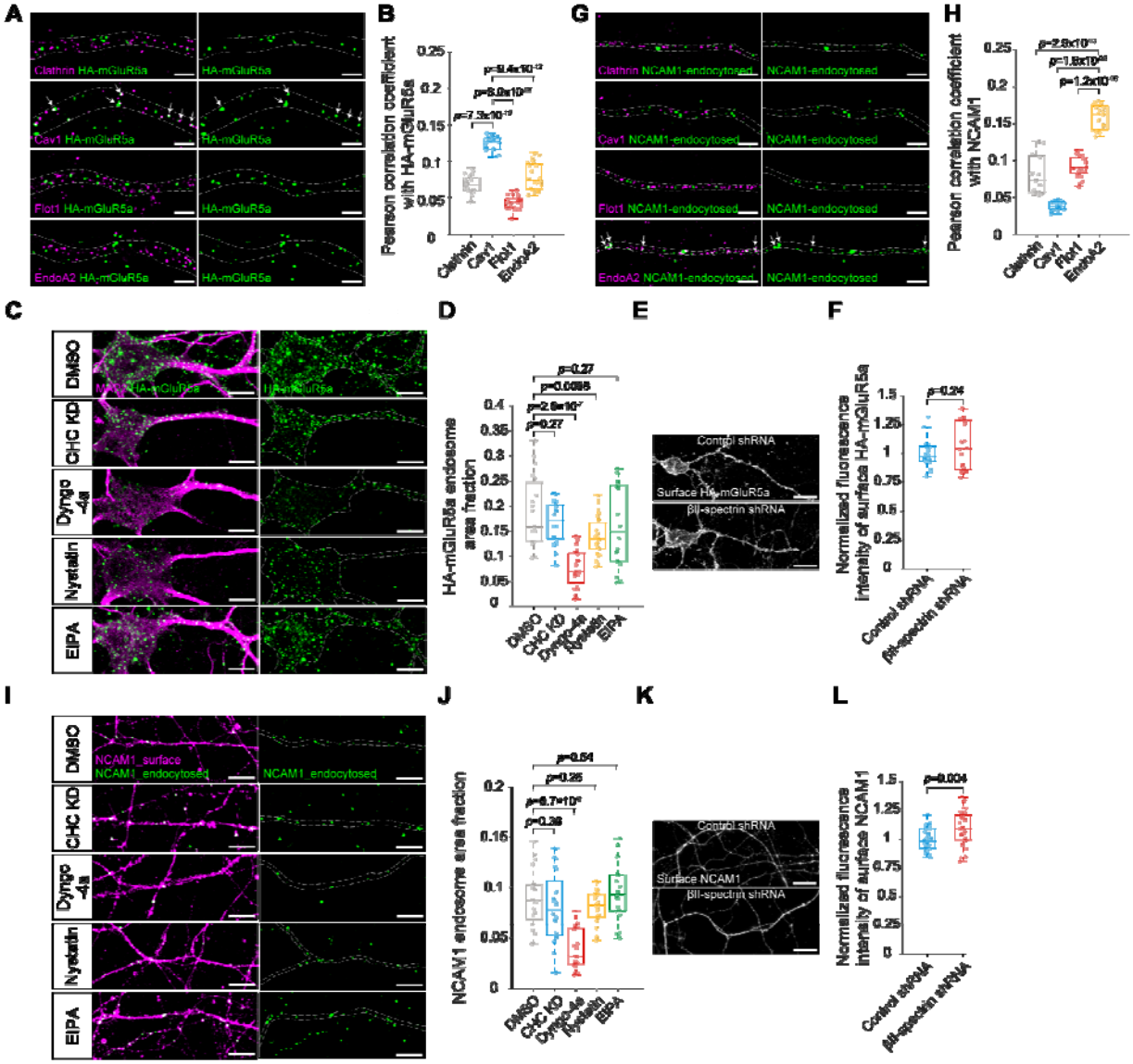

Fig. S7. Endocytic pathways for HA-mGluR5a and NCAM1 endocytosis, related to Fig. 4. (**A**) Dual-color SIM images of internalized HA-mGluR5a (green) and endocytic pits (magenta; clathrin, Cav1, Flot1 or EndoA2) in dendrites of WT neurons overexpressing HA-mGluR5a treated with anti-HA antibody for 30 minutes. Regions of strong colocalization are indicated by white arrows. Scale bars: 2 µm. (**B**) Pearson correlation coefficients between internalized HA-mGluR5a and endocytic pits. (**C**) Confocal fluorescence images of MAP2 (magenta) and internalized HA-mGluR5a (green) in the somatodendritic regions of CHC KD neurons overexpressing HA-mGluR5a pretreated with DMSO, followed by treatment with anti-HA antibody for 40 minutes, and WT neurons overexpressing HA-mGluR5a pretreated with DMSO, dyngo-4a, nystatin or EIPA for 30 minutes, followed by treatment with anti-HA antibody for 40 minutes. Scale bars: 10 µm. (**D**) Boxplots of HA-mGluR5a endocytosis in somatodendritic regions of neurons, quantified by the area fraction of HA-mGluR5a endosomes. (**E**) Widefield epi-fluorescence images of surface-localized HA-mGluR5a in WT and βII-spectrin KD neurons without ligand stimulation. Surface-localized HA-mGluR5a was immunostained with anti-HA antibody following cell fixation without Triton permeabilization. Scale bars: 25 µm. (**F**) Boxplots showing the normalized fluorescence intensity of surface HA-mGluR5a. (**G**) Dual-color SIM images of internalized NCAM1 (green) and

endocytic pits (magenta; clathrin, Cav1, Flot1 or EndoA2) in axons of WT neurons treated with anti-NCAM1 antibody for 30 minutes. Regions of strong colocalization are indicated by white arrows. Scale bars, 2 µm. (**H**) Pearson correlation coefficients between internalized NCAM1 and endocytic pits. (**I**) Confocal fluorescence images of surface NCAM1 and internalized NCAM1 in CHC KD neurons pretreated with DMSO, followed by treatment with anti-NCAM1 antibody for 40 minutes, and WT neurons pretreated with DMSO, dyngo-4a, nystatin or EIPA for 30 minutes, followed by treatment with anti-NCAM1 antibody for 40 minutes. Scale bars: 10 µm. (**J**) Boxplots of NCAM1 endocytosis in neurons, quantified by the area fraction of NCAM1 endosomes. (**K**) Widefield epi-fluorescence images of surface-localized NCAM1 in WT and βII-spectrin KD neurons without ligand stimulation. Surface-localized NCAM1 was immunostained with anti-NCAM1 antibody following cell fixation without Triton permeabilization. Scale bars: 15 µm. (**L**) Boxplots showing the normalized fluorescence intensity of surface NCAM1. Boxplots show the median and boundaries (first and third quartile); Whiskers denote 1.5 times the interquartile range of the box. *p*-values calculated with two-sided unpaired Student's *t*-test.

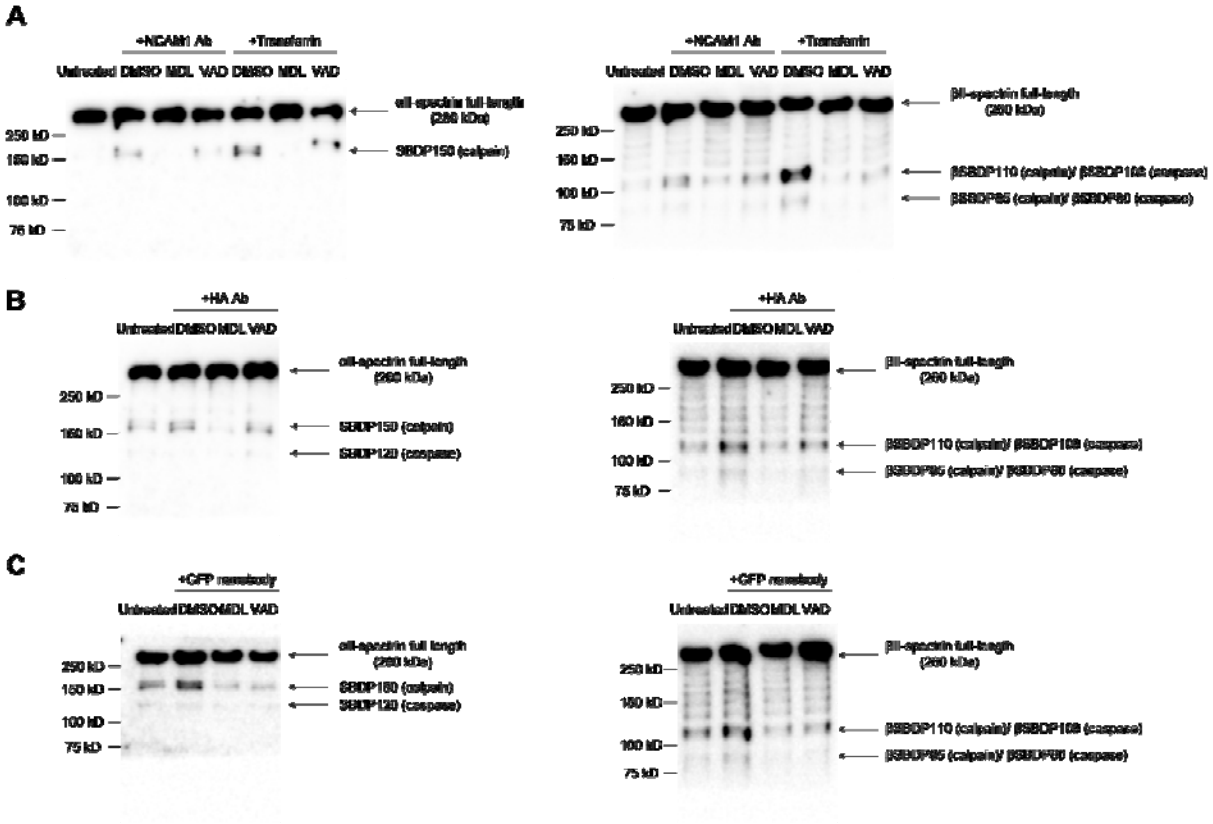

Fig. S8. Western blot analysis of MPS degradation triggered by ligand-induced endocytosis, related to Fig. 5. (**A**) Left: Immunoblot detection of αII-spectrin cleavage in WT neurons treated with anti-NCAM1 antibody or CF568-transferrin for 60 minutes. For inhibitor conditions, neurons were pretreated with MDL or VAD prior to ligand-induced endocytosis. Right: Same as Left, but for βII-spectrin cleavage. (**B**) Left: Immunoblot detection of αII-spectrin cleavage in neurons overexpressing HA-mGluR5a treated with anti-HA antibody for 60 minutes. For inhibitor conditions, neurons were pretreated with MDL or VAD prior to ligand-induced endocytosis. Right: Same as Left, but for βII-spectrin cleavage. (**C**) Left: immunoblot detection of αII-spectrin cleavage in neurons overexpressing SEP-APP treated with GFP nanobody for 60 minutes. For inhibitor conditions, neurons were pretreated with MDL or VAD prior to ligand-induced endocytosis. Right: Same as Left, but for βII-spectrin cleavage.

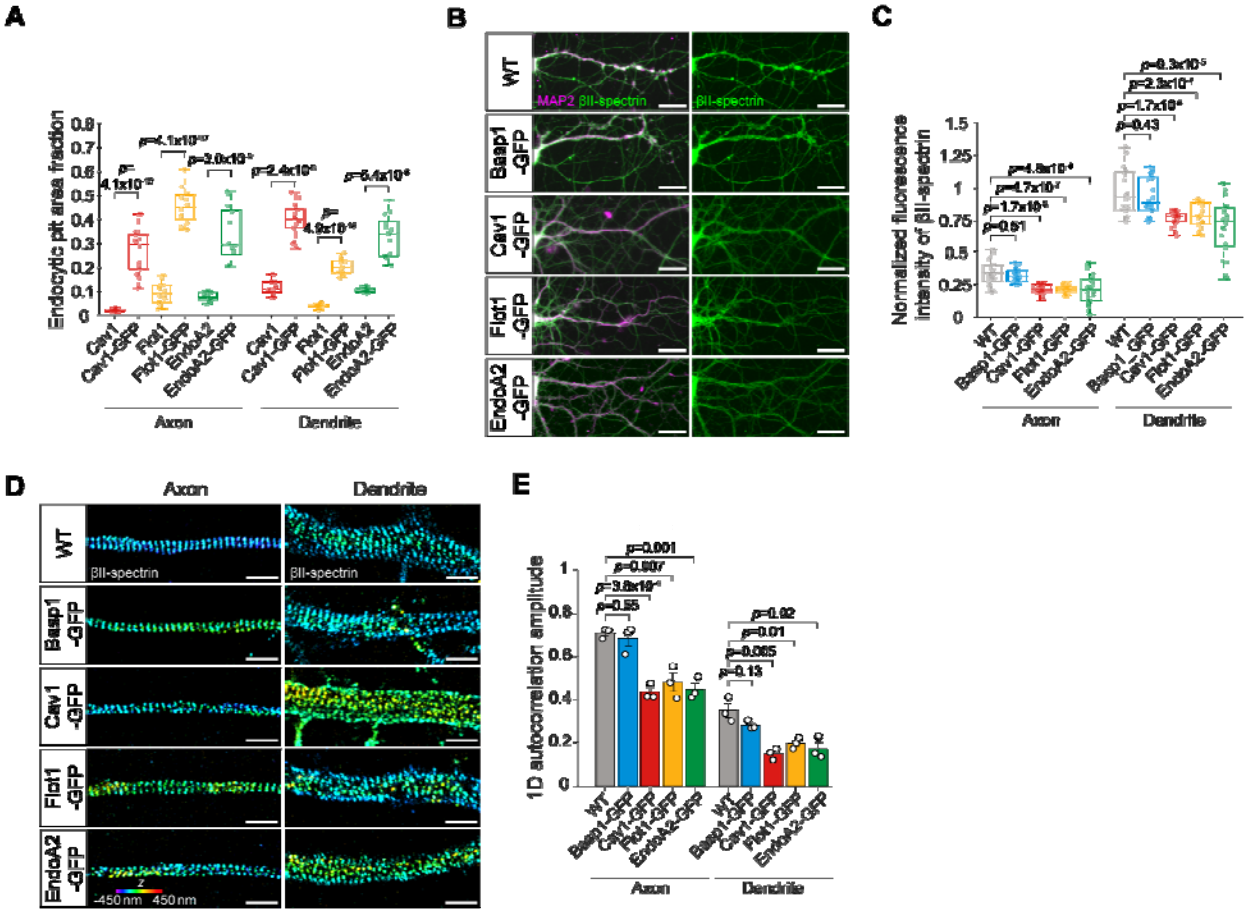

Fig. S9. Overexpression of endocytic proteins partially degrades the MPS in neurons, related to Fig. 5. (**A**) Boxplots of the area fraction of endogenous and overexpressed endocytic pits in axonal and dendritic neuronal compartments, quantified from the STORM data shown in Figs. 2 and 3, and Figs. S5. (**B**) Widefield epi-fluorescence images of MAP2 (magenta) and βII-spectrin (green) in WT neurons, and neurons overexpressing Basp1, Cav1, Flot1, and EndoA2. Scale bars, 25 µm. (**C**) Boxplots of normalized fluorescence intensity of βII-spectrin in axons and dendrites of neurons. (**D**) 3D STORM images of immunostained βII-spectrin in axons and dendrites of WT neurons, and neurons overexpressing Basp1, Cav1, Flot1, and EndoA2. Scale bars, 1 µm. Color scale bar represents the z-coordinate information. (**E**) Averaged 1D autocorrelation amplitude of βII-spectrin in axons and dendrites of neurons. Boxplots show the median and boundaries (first and third quartile); Whiskers denote 1.5 times the interquartile range of the box. *p*-values calculated with two-sided unpaired Student's *t*-test.

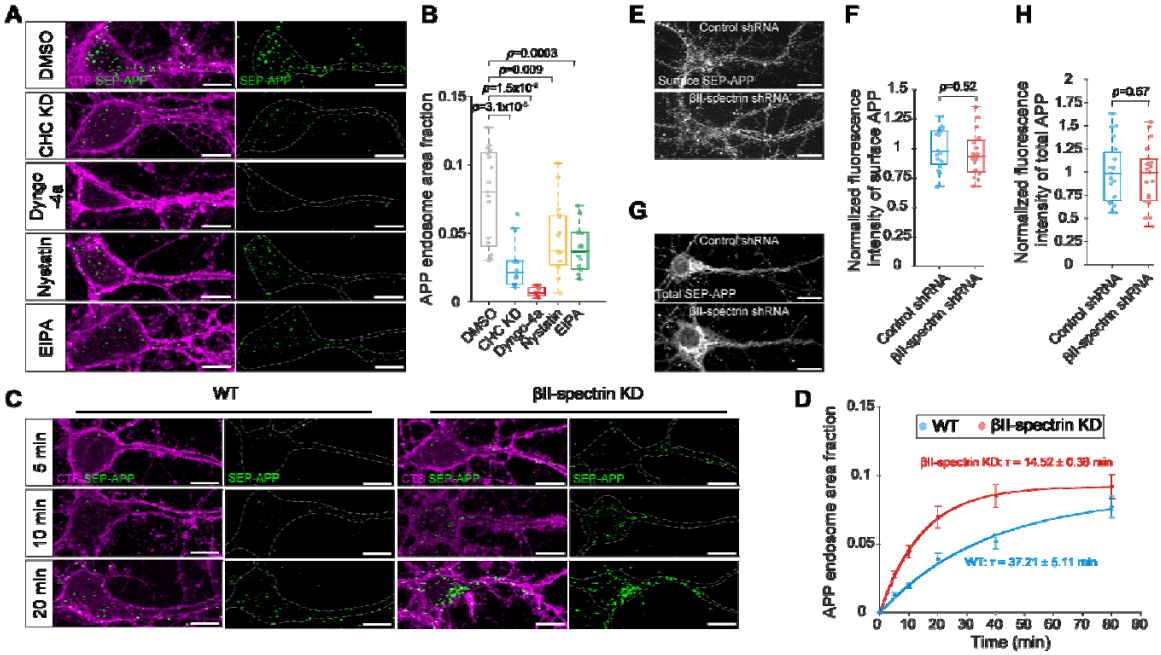

Fig. S10. Endocytic pathways of APP endocytosis, related to Fig. 6. (**A**) Confocal fluorescence images of CTB (magenta) and internalized SEP-APP (green) in somatodendritic regions of CHC KD neurons overexpressing SEP-APP pretreated with DMSO, followed by GFP nanobody treatment for 40 minutes, and WT neurons overexpressing SEP-APP pretreated with DMSO, dyngo-4a, nystatin, or EIPA for 30 minutes, followed by GFP nanobody treatment for 40 minutes. Scale bars: 10 µm. (**B**) Boxplots of SEP-APP endocytosis in somatodendritic regions of neurons, quantified by the area fraction of SEP-APP endosomes. (**C**) Left: Confocal fluorescence images of CTB (magenta) and internalized SEP-APP in somatodendritic region of WT neurons overexpressing SEP-APP treated with GFP nanobody for 5, 10, and 20 minutes. Right: Same as Left, but in βII-spectrin KD neurons. Scale bars: 10 µm. (**D**) Time course of APP endocytosis in the somatodendritic regions of WT and βII-spectrin KD neurons, quantified by the area fraction of APP endosomes. Solid lines represent single-exponential fits to the data. Data are presented as mean ± s.e.m. (**E**) Widefield epi-fluorescence images of surface-localized SEP-APP in WT and βII-spectrin KD neurons without ligand stimulation. Surface-localized SEP-APP was immunostained with anti-GFP antibody following cell fixation without Triton permeabilization. Scale bars: 25 µm. (**F**) Boxplots showing the normalized fluorescence intensity of surface SEP-APP. Boxplots show the median and boundaries (first and third quartile); Whiskers denote 1.5 times the interquartile range of the box. *p*-values calculated with two-sided unpaired Student's *t*-test. (**G**) Widefield epi-fluorescence images of total SEP-APP in WT and βII-spectrin KD neurons without ligand stimulation. Total SEP-APP was immunostained with anti-GFP antibody following cell fixation and Triton permeabilization. Scale bars: 25 µm. (**H**) Boxplots showing the normalized fluorescence intensity of total SEP-APP. Boxplots show the median and boundaries (first and third quartile); Whiskers denote 1.5 times the interquartile range of the box. *p*-values calculated with two-sided unpaired Student's *t*-test.